

# High-frequency gravitational wave transients from superradiance

Henry Su,<sup>a</sup> Lucas Brown,<sup>b,c</sup> Christopher Ewasiuk,<sup>b,c</sup> and Stefano Profumo<sup>b,c</sup>

<sup>a</sup>Department of Physics, University of Massachusetts, Amherst, MA 01003, USA

<sup>b</sup>Department of Physics, University of California, Santa Cruz  
Santa Cruz, CA, 95064, USA

<sup>c</sup>Santa Cruz Institute for Particle Physics, University of California, Santa Cruz  
Santa Cruz, CA, 95064, USA

**Abstract.** Ultralight bosons can form macroscopic gravitational-atom clouds around rotating black holes via superradiance, sourcing quasi-monochromatic gravitational waves through level transitions and annihilation. Primordial black holes provide a natural setting for such systems in a frequency range relevant for resonant-cavity experiments. We present a unified treatment of gravitational-wave emission from both isolated and binary-perturbed gravitational atoms in this regime. For isolated systems, we derive analytic expressions for the time- and frequency-domain strain from transition and annihilation channels, emphasizing their narrow-band structure. For binaries, we model resonantly driven level transitions using the Landau–Zener formalism and compute the resulting transient signals. We find that, while binary-driven transitions generically yield signals with durations compatible with detector response times, their characteristic strain lies well below the sensitivity of current experiments at astrophysically plausible distances, and event rates further suppress detectability by requiring sources at unrealistically small separations. We quantify the improvements in sensitivity, bandwidth, and response needed to render these signals observable, and identify gravitational-atom systems around primordial black holes as a theoretically well-motivated target for future high-frequency gravitational-wave searches.

---

## Contents

<b>1</b>	<b>Introduction</b>	<b>2</b>
<b>2</b>	<b>Superradiance and the Parameter Space for High-Frequency GWs</b>	<b>4</b>
2.1	Bound States, Regge Trajectories, and the GW Frequency Map	4
2.2	Superradiant Instability Rates and Growth Timescales	7
2.3	Cloud Saturation and Bosenova Cycling	8
<b>3</b>	<b>Gravitational-Wave Signatures from Isolated Gravitational Atoms</b>	<b>10</b>
3.1	Gravitational Waves from Level Transitions	10
3.1.1	Two-level population dynamics	10
3.1.2	Time-domain gravitational-wave strain	12
3.1.3	Saturation occupation number and peak strain	13
3.1.4	Signal lifetime	13
3.2	Gravitational Waves from Boson Annihilation	13
3.2.1	Annihilation frequency and rate	13
3.2.2	Time-domain occupation number and strain	14
3.2.3	Peak strain scaling	15
3.2.4	Signal lifetime and detectability window	15
3.3	Summary and comparison of isolated-GA signals	16
<b>4</b>	<b>Gravitational-Wave Signatures from Gravitational Atoms in Binaries</b>	<b>16</b>
4.1	Time- and Frequency-Domain Waveforms	17
4.2	Parameter Space Constraints	18
4.3	Detectability Prospects for PBH Gravitational-Atom Binaries	19
4.3.1	Peak-frequency map in the PBH mass range	19
4.3.2	Benchmark waveform and ring-up criterion	20
4.3.3	ADMX sensitivity comparison	21
4.4	Doppler Frequency Shift for Solar-System Flybys	23
<b>5</b>	<b>Prospects for Observation at High-Frequency Gravitational-Wave Detectors</b>	<b>23</b>
5.1	Merger Rate from the Early Two-Body Formation Channel	24
5.2	Dichromatic Mass Function and Event Rates	24
5.3	Characteristic Detection Distance and the Strain Gap	25
5.4	Implications for Future Detectors	27
<b>6</b>	<b>Discussion and Conclusions</b>	<b>27</b>
6.1	Summary and Key Conclusions	27
6.2	Comparison to Related Work	28
6.3	Caveats and Limitations	29
6.4	Outlook and Future Directions	30

<b>A</b>	<b>Frequency Domain Strain Templates</b>	<b>31</b>
A.1	Annihilation Strain	32
A.2	Isolated Level Transition Strain	34
A.3	Binary Level Transition Strain	36

---

## 1 Introduction

The question of which physical mechanisms can produce gravitational waves (GWs) in the MHz–GHz band has gained renewed urgency with the recent development of resonant-cavity and broadband electromagnetic detectors sensitive to oscillatory metric perturbations at these frequencies [1–3]. Unlike the audio-band signals detected by LIGO/Virgo/KAGRA or the mHz signals targeted by LISA, high-frequency GWs cannot be sourced by stellar-mass compact binary mergers, and the landscape of viable production mechanisms is far less explored. Among the handful of well-motivated theoretical candidates, black-hole superradiance stands out because it can be made quantitative, is tied to motivated extensions of the Standard Model, and—as we show in this paper—naturally places signals in the GHz band when the black holes involved are of primordial origin and the boson masses are in a range motivated, for example, by the QCD axion phenomenology [4–10]. We choose to use natural units  $\hbar = c = 1$  throughout this paper.

The basic mechanism is as follows. A bosonic field of mass  $\mu$  satisfying the superradiant condition

$$0 < \omega < m \Omega_H, \quad (1.1)$$

where  $\Omega_H$  is the angular velocity of the Kerr horizon and  $m$  the azimuthal quantum number, is exponentially amplified at the expense of the black hole’s rotational energy [11–13]. When the boson’s Compton wavelength is comparable to the gravitational radius, the amplified modes are gravitationally trapped and grow into a macroscopic quasi-bound cloud—a *gravitational atom* (GA)—with occupation numbers reaching  $N \sim 10^{70}$ – $10^{80}$  [14, 15]. The dynamics are controlled by the gravitational fine-structure constant

$$\alpha \equiv GM_{\text{BH}} \mu, \quad (1.2)$$

which simultaneously sets the cloud radius  $r_c \sim M_{\text{BH}}/\alpha^2$ , the superradiant instability rate, and the hydrogenic spectrum of bound levels [16, 17]. Efficient growth requires  $\alpha \sim 0.1$ – $0.5$ , which, for a given boson mass  $\mu$ , selects a preferred BH mass—or equivalently, for a given BH mass, a preferred range of boson masses.

The GW frequency is set almost entirely by  $\mu$ : annihilation of two cloud bosons into a graviton emits at  $\omega_{\text{ann}} \simeq 2\mu$ , while level transitions between states with principal quantum numbers  $n_g$  and  $n_e$  emit at the Bohr frequency  $\omega_{\text{tr}} \propto \mu\alpha^2(n_g^{-2} - n_e^{-2})$ . For stellar-mass BHs this places signals in the audio band probed by LIGO/Virgo/KAGRA, and an extensive literature has explored these GW signatures and the spin constraints they imply [15, 17–21]. A qualitatively distinct regime arises for *primordial black holes* (PBHs) [22–24]. For sub-solar mass PBH masses the superradiance condition selects boson masses  $\mu \sim 10^{-7}$ – $10^{-5}$  eV, driving GW emission into the MHz–GHz band. This is precisely the frequency range targeted by resonant-cavity haloscopes such as ADMX, which were originally designed to search for axion dark matter but are equally sensitive to oscillatory strain at GHz frequencies, provided the signal persists for longer than the cavity ring-up time  $\tau_{\text{ring}} \sim 1/\Delta f_{\text{band}}$ . Also, notably,

bosons in that mass range are independently motivated by the axion solution to the strong CP problem [4–6] and the cosmology thereof [7–10].

Once a cloud has formed and superradiance saturates, two emission channels become active in the isolated system:

1. *Level transitions*, in which the quadrupole self-interaction of two populated states drives bosons from an excited level to a lower one, emitting quasi-monochromatic GWs at the Bohr frequency  $\omega_{\text{tr}}$ .
2. *Annihilations*, in which pairs of bosons convert into gravitons at  $\omega_{\text{ann}} \simeq 2\mu$ , producing an extremely long-lived, slowly decaying quasi-monochromatic signal.

These signals have been studied in detail for isolated stellar-mass GAs, and we extend that framework here to the PBH mass range and the associated GHz frequency band [15, 17, 18]. Bosenova collapses, in which the cloud implodes once its occupation number exceeds a critical value set by bosonic self-interactions, introduce additional burst-like GW emission and periodically reset the superradiant growth [25, 26]; we account for the resulting upper bound on cloud populations when deriving strain amplitudes.

In realistic astrophysical environments, however, GAs are often not isolated. A binary companion introduces a time-varying tidal potential that drives resonant transitions between GA levels whenever the orbital frequency sweeps through a Bohr frequency of the gravitational atom. In this regime the cloud behaves as a driven two-level system, and its response is captured by a Landau–Zener analysis [27, 28]: depending on the adiabaticity parameter  $z \equiv \eta^2/(\Delta m|\dot{\Omega})$ , where  $\eta$  is the tidal mixing amplitude, transitions range from partial population transfer ( $z \ll 1$ ) to complete level inversion ( $z \gg 1$ ). The resulting GW signal is a short-duration transient burst whose characteristic strain and spectral shape have recently been computed by Kyriazis & Yang [29], whose formalism we adopt and apply to the PBH binary case. Binary-induced resonant transitions also imply:

- rapid depletion of the cloud, shortening or quenching the long-lived annihilation and transition signals;
- additional transient GW components at the resonance frequency, superimposed on the binary inspiral signal; and
- modifications to the binary’s inspiral rate, including the possibility of “floating orbits” where cloud-mediated energy loss competes with GW radiation [15, 28].

Systematic studies of such binary-perturbed GAs have been carried out for stellar-mass BH binaries and extreme mass-ratio inspirals relevant for LISA [27, 28, 30–32]. The present work extends this program to PBH masses and GHz frequencies, a regime not previously treated in a unified framework.

In this paper we bring together four ingredients that have not previously been combined in the context of high-frequency GWs: (i) relativistic superradiant instability rates [33, 34], (ii) numerically computed cloud masses [35, 36], (iii) the binary-induced resonance formalism of Ref. [29], and (iv) realistic ADMX sensitivity curves [1]. Concretely, we make the following contributions:

- We map the superradiant parameter space in the PBH mass range using Regge trajectories (Sec. 2), identifying the  $(\mu, M_{\text{BH}}, \alpha)$  combinations that produce MHz–GHz

emission and assessing the role of bosonova saturation and accretion in bounding the allowed cloud populations.

- For isolated GAs we derive time-domain GW strain envelopes and analytic closed-form frequency-domain templates, via the exponential integral  $E_1$ , for both the level-transition and annihilation signals (Sec. 3 and App. A). We find that peak strains can reach  $h \sim 10^{-22}$  at 1 kpc for the most optimistic configurations of the annihilation channel, while level-transition signals typically peak at  $h \sim 10^{-23}$  and can be significantly smaller for specific benchmark configurations.
- For PBH binaries we apply the Landau-Zener formalism to the hyperfine transition  $\{2, 1, 1\} \rightarrow \{2, 1, -1\}$ , compute the transient GW burst characteristic strain across the  $M_{\text{BH}}\text{-}\alpha$  parameter space (Sec. 4), and derive the conditions under which the signal duration exceeds the ADMX ring-up time.
- We provide a detectability analysis for ADMX (Sec. 5), showing that despite satisfying the ring-up time criterion, the binary-induced burst strain falls orders of magnitude below the ADMX sensitivity threshold at astrophysically plausible distances. Using PBH merger rates from the early two-body formation channel [37], we determine that detectable events would need to occur at  $\lesssim 1$  AU, whereas the merger rate implies characteristic event distances exceeding  $\sim 9$  kpc.

Taken together, our results show that PBH-gravitational atom systems are among the very few theoretically well-motivated sources of MHz–GHz gravitational waves, but that a significant improvement in detector strain sensitivity—beyond the reach of current ADMX runs—is required to make them observable. We identify the combination of better sensitivity, faster ring-up times, and lower frequency coverage as the priority for future high-frequency GW detector design. Our analytic frequency-domain templates provide concrete waveform targets for such searches.

## 2 Superradiance and the Parameter Space for High-Frequency GWs

Rotating black holes interacting with ultralight bosonic fields define a structured parameter space in which GW emission frequencies are tied directly to the masses of both the black hole and the boson. This section establishes the parametric foundation for the rest of the paper. We derive the conditions for superradiant bound-state formation, introduce the Regge trajectories that delimit the allowed region, give the instability rate governing cloud growth, and identify the portion of parameter space that produces MHz–GHz gravitational waves.

The central result—summarized graphically in Fig. 1—is that the MHz–GHz window is populated by black holes in the primordial mass range  $M_{\text{BH}} \sim 10^{-6} - 10^{-3} M_{\odot}$  for boson masses  $\mu \sim 10^{-8} - 10^{-5}$  eV and gravitational coupling  $\alpha \sim 0.1 - 0.3$ , as appropriate for efficient superradiance.

### 2.1 Bound States, Regge Trajectories, and the GW Frequency Map

A massive scalar boson of mass  $\mu$  on a Kerr background admits quasi-bound states whenever its Compton wavelength  $\bar{\lambda}_C = \mu^{-1}$  (in natural units  $\hbar = c = 1$ ) is comparable to the gravitational radius  $r_g \equiv GM_{\text{BH}}$ . The ratio of these two scales is the gravitational fine-structure constant

$$\alpha \equiv \frac{r_g}{\bar{\lambda}_C} = GM_{\text{BH}} \mu. \quad (2.1)$$

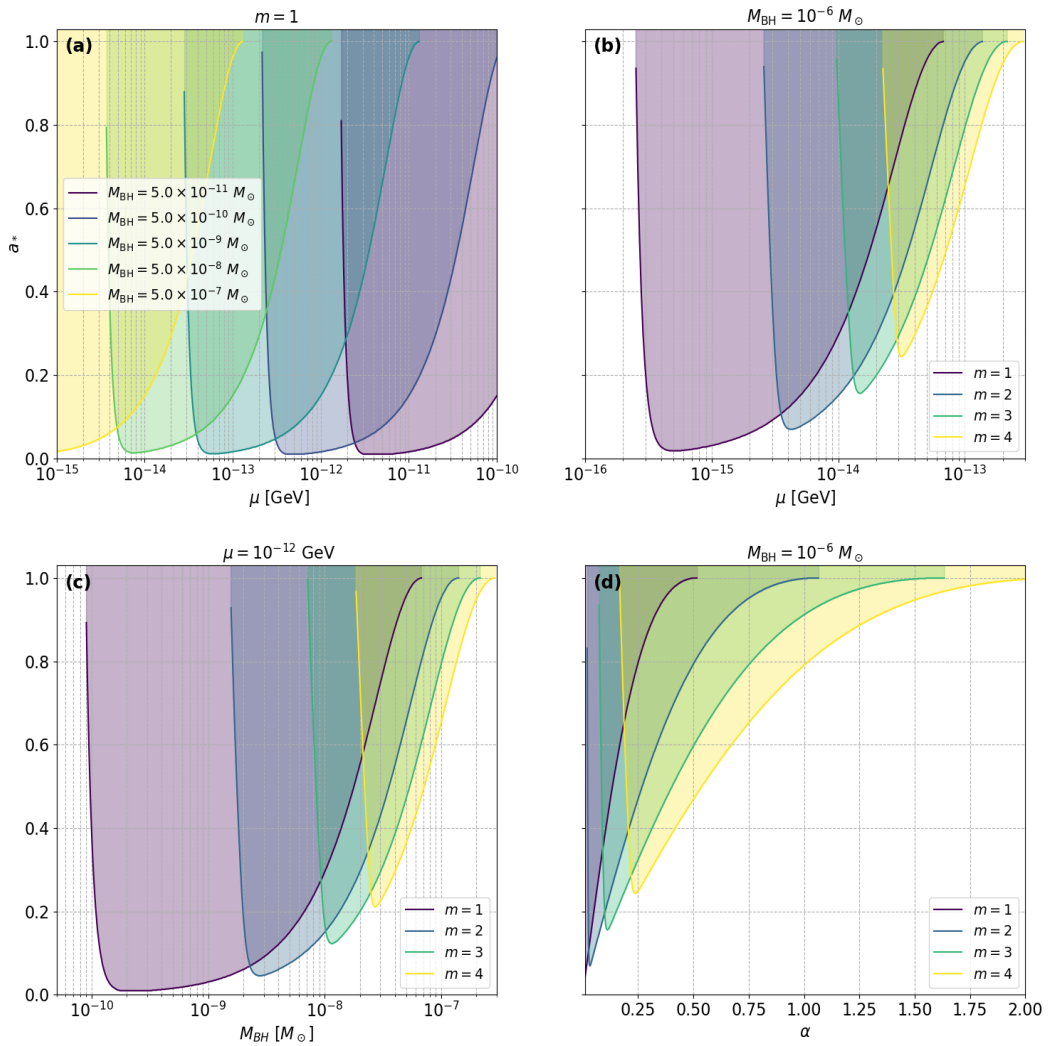


**Figure 1:** Regge trajectories showing the minimum black hole spin  $a_*$  required to sustain superradiant growth as a function of boson and black hole parameters, for azimuthal modes  $m = 1, 2, 3, 4$ . Shaded regions indicate parameter space where superradiance is active. **(a)** Superradiance threshold as a function of boson mass  $\mu$  for fixed  $m = 1$  and varying black hole mass  $M$ . **(b)** Threshold as a function of  $\mu$  for fixed  $M = 10^{-6} M_\odot$  and varying  $m$ . **(c)** Threshold as a function of  $M_{\text{BH}}$  for fixed boson mass  $\mu = 10^{-3} \text{ eV}$  and varying  $m$ . **(d)** Threshold as a function of the gravitational coupling  $\alpha = M\mu$  for fixed  $M = 10^{-6} M_\odot$  and varying  $m$ .

In the limit  $\alpha \ll 1$  the quasi-bound spectrum is precisely hydrogenic [14, 38]:

$$\omega_n \simeq \mu \left( 1 - \frac{\alpha^2}{2n^2} \right), \quad (2.2)$$

where  $n$  is the principal quantum number. The spatial extent of the cloud in state  $\{n, \ell, m\}$  is

$$r_c = \frac{n^2}{\alpha^2} r_g = \frac{n^2}{\mu\alpha}, \quad (2.3)$$

so the cloud becomes more diffuse at smaller  $\alpha$ . The regime  $\alpha \sim 0.1\text{--}0.5$  simultaneously ensures that the cloud is compact enough for efficient angular-momentum extraction and energetic enough for detectable GW emission; both smaller and larger  $\alpha$  values suppress the instability rate exponentially, as discussed in Sec. 2.2.

Superradiance is active when the bound-state frequency satisfies the *superradiant condition*

$$\omega < m\Omega_H, \quad (2.4)$$

where  $m$  is the azimuthal quantum number and  $\Omega_H = a_*/[2GM_{\text{BH}}(1 + \sqrt{1 - a_*^2})]$  is the angular velocity of the Kerr horizon [15], with  $a_*$  the dimensionless BH spin. Substituting the leading-order binding energy  $\omega \approx \mu$  into Eq. (2.4) and solving for the critical spin, one finds the threshold

$$a_*^{\text{crit}}(\alpha, m) = \frac{4m\alpha}{m^2 + 4\alpha^2}, \quad (2.5)$$

above which superradiance operates ( $a_* > a_*^{\text{crit}}$ ) and below which it does not. This threshold defines the *Regge trajectory* of the mode: the curve  $a_* = a_*^{\text{crit}}(\alpha, m)$  in the  $(a_*, \alpha)$  plane, or equivalently in the  $(a_*, M_{\text{BH}})$  or  $(a_*, \mu)$  planes for fixed  $\mu$  or  $M_{\text{BH}}$ . A BH that forms with spin above a Regge trajectory will be driven toward it by superradiant spin-down; at the trajectory, growth saturates.

In the limit  $a_* \rightarrow 1$  (maximally spinning BH), Eq. (2.5) gives  $a_*^{\text{crit}} \rightarrow 1$  when  $\alpha \rightarrow m/2$ , so the hard upper bound for superradiance to be possible at all is

$$\alpha < \frac{m}{2}. \quad (2.6)$$

This bound is visible in all four panels of Fig. 1 as the right-hand edge of each shaded superradiant region.

Figure 1 presents the Regge trajectories across four complementary slices of parameter space. In each panel the shaded area marks the region where a given mode can grow:

- *Top-left*: the  $(\mu, a_*)$  plane for varying  $M_{\text{BH}}$  at fixed  $m = 1$ . The allowed region shifts to larger boson masses as  $M_{\text{BH}}$  decreases, illustrating that lighter PBHs couple to heavier bosons at the same  $\alpha$ .
- *Top-right and bottom-left*: the  $(\mu, a_*)$  and  $(M_{\text{BH}}, a_*)$  planes for fixed host BH mass and varying  $m$ . Higher azimuthal number extends the superradiant region to larger  $\alpha$  per Eq. (2.6), but requires larger initial BH spins for the mode to grow.
- *Bottom-right*: the  $(\alpha, a_*)$  plane at fixed  $M_{\text{BH}}$ , showing the Regge trajectories in their most natural parametrization. The state with  $m = \ell = 1$  has the smallest critical spin at given  $\alpha$  and therefore begins extracting angular momentum earliest.

Throughout, quantum numbers are taken to satisfy  $m = \ell = n - 1$  (the lowest radial mode of each angular sector), since these states have the largest angular momentum content per unit energy and therefore achieve the highest saturation occupation numbers [15, 16].

**Table 1:** Mapping between boson mass  $\mu$ , host BH mass at  $\alpha = 0.2$ , and annihilation GW frequency  $f_{\text{ann}}$ . The ADMX Run 1 data-collection band (0.645–1.4 GHz) lies between the third and fourth rows, with the corresponding frequencies bracketing the experimental sensitivity range.

$\mu$	$M_{\text{BH}}/M_{\odot}$	$f_{\text{ann}}$	Band
$10^{-9}$ eV	$2.7 \times 10^{-2}$	480 Hz	LIGO/Virgo audio
$10^{-7}$ eV	$2.7 \times 10^{-4}$	48 MHz	HF (broadband RF)
$10^{-6}$ eV	$2.7 \times 10^{-5}$	484 MHz	~ADMX Run 1 (lower)
$3 \times 10^{-6}$ eV	$9 \times 10^{-6}$	1.45 GHz	ADMX Run 1 (upper)
$10^{-5}$ eV	$2.7 \times 10^{-6}$	4.8 GHz	Next-generation RF

The gravitational-wave emission frequencies are set by  $\mu$  through two distinct channels. For *annihilation* of two cloud bosons into a single graviton:

$$f_{\text{ann}} = \frac{\omega_{\text{ann}}}{2\pi} \simeq \frac{\mu}{\pi} \approx 484 \text{ MHz} \left( \frac{\mu}{10^{-6} \text{ eV}} \right). \quad (2.7)$$

For a *level transition* from principal quantum number  $n_e$  down to  $n_g$ :

$$f_{\text{tr}} = \frac{\omega_{\text{tr}}}{2\pi} \simeq \frac{\mu\alpha^2}{4\pi} \left( \frac{1}{n_g^2} - \frac{1}{n_e^2} \right) \approx 121 \text{ MHz} \left( \frac{\mu}{10^{-6} \text{ eV}} \right) \left( \frac{\alpha}{0.2} \right)^2 \left( \frac{1}{n_g^2} - \frac{1}{n_e^2} \right). \quad (2.8)$$

The MHz–GHz frequency window therefore corresponds to boson masses  $\mu \sim 10^{-8}$ – $10^{-5}$  eV via annihilation, or to slightly heavier bosons when transitions are the dominant channel. The black hole mass required for superradiance efficiency to peak at  $\alpha \simeq 0.2$  is then

$$M_{\text{BH}} \simeq \frac{\alpha}{\mu G} \approx 2.7 \times 10^{-5} M_{\odot} \left( \frac{\alpha}{0.2} \right) \left( \frac{10^{-6} \text{ eV}}{\mu} \right), \quad (2.9)$$

Across the range  $\mu \sim 10^{-8} - 10^{-5}$  eV relevant for MHz–GHz emission, this corresponds to black hole masses  $M_{\text{BH}} \sim 10^{-6} - 10^{-3} M_{\odot}$  for  $\alpha \sim 0.1 - 0.3$ . This is the PBH mass range, establishing the central connection exploited throughout this paper: *high-frequency GW detectors such as ADMX are natural instruments for probing ultralight bosons through superradiance around PBHs*. For reference, Table 1 displays this mapping for frequencies spanning from the LIGO audio band to the GHz range. This illustrates that the MHz–GHz frequency range associated with superradiant gravitational atoms spans and extends beyond the current ADMX sensitivity window, motivating broader frequency coverage in future high-frequency gravitational-wave searches.

## 2.2 Superradiant Instability Rates and Growth Timescales

The cloud occupation number grows as  $\dot{N} = \Gamma_{nlm} N$ , where  $\Gamma_{nlm} = \text{Im}(\omega)$  is the superradiant instability rate. In the non-relativistic limit ( $\alpha \ll 1$ ) this rate can be computed analytically by matched-asymptotic methods [14, 15, 38]:

$$\Gamma_{nlm} \simeq \frac{C_{nlm}(a_*)}{r_g} \alpha^{4\ell+5}, \quad (2.10)$$

where  $C_{nlm}(a_*)$  is a dimensionless, spin-dependent coefficient. For the dominant  $\{2, 1, 1\}$  state [38]

$$C_{211}(a_*) \approx \frac{a_*}{48} \left(1 - \frac{4\alpha^2}{a_*^2 m^2}\right)^{1/2}, \quad (2.11)$$

which vanishes at the superradiance threshold  $\alpha \rightarrow a_* m/2$  and is maximized at intermediate spin. The  $\alpha^{4\ell+5}$  dependence makes higher- $\ell$  modes exponentially slower: at  $\alpha = 0.2$ , the  $\ell = 2$  state grows  $\sim \alpha^4 \simeq 1.6 \times 10^{-3}$  times more slowly than the  $\ell = 1$  dominant mode. Accordingly, the  $\{2, 1, 1\}$  state is almost always the first to saturate, and it determines the timescale on which angular momentum is extracted from the BH.

The  $e$ -folding time for cloud growth is

$$\tau_{\text{SR}} \equiv \Gamma_{nlm}^{-1} \approx 5 \text{ s} \left(\frac{M_{\text{BH}}}{10^{-5} M_{\odot}}\right) \left(\frac{0.2}{\alpha}\right)^9 \left(\frac{0.1}{C_{211}}\right), \quad (2.12)$$

using  $r_g/c \simeq 5 \times 10^{-6} \text{ s} (M_{\text{BH}}/M_{\odot})$  for the light-crossing time. Figure 2a shows  $\tau_{\text{SR}}$  in years as a function of  $\alpha$  for modes  $\ell = m = 1, \dots, 4$ ; Fig. 2b shows the same rate in geometrized units  $r_g \Gamma_{nlm}$ , making the  $\ell$ -dependent peak structure visible.

Three features of these figures are particularly relevant to our analysis:

1. *Steep  $\alpha$ -dependence at small  $\alpha$ .* Because  $\tau_{\text{SR}} \propto \alpha^{-(4\ell+5)}$ , the growth time rises by many orders of magnitude as  $\alpha$  decreases below  $\sim 0.1$ . For the ADMX-relevant PBH mass range,  $\tau_{\text{SR}}$  ranges from seconds at  $\alpha \sim 0.4$  to timescales exceeding the Hubble time at  $\alpha \lesssim 0.05$ . This sets a practical lower bound  $\alpha \gtrsim 0.05$  for any detectable cloud to have formed.
2. *Cutoff at the superradiance threshold.* Both figures show  $\Gamma_{nlm} \rightarrow 0$  as  $\alpha \rightarrow m/2$ , because the superradiant enhancement  $C_{nlm}$  vanishes there. The instability therefore operates within a finite window  $\alpha \in (0.05, m/2)$ , peaking at  $\alpha \sim 0.2$ – $0.3$ .
3. *Multi-mode competition.* For sufficiently high initial BH spin, several  $m$ -modes can satisfy the superradiance condition simultaneously. Although the  $m = 1$  mode dominates the growth rate, modes with  $m \geq 2$  develop non-negligible populations over long timescales, contributing sub-dominant but non-zero GW channels at their respective transition and annihilation frequencies.

Throughout Secs. 3 and 4 we use relativistic instability rates from Refs. [33, 34] rather than the leading-order non-relativistic form of Eq. (2.10), in order to capture the quantitatively important relativistic corrections at  $\alpha \sim 0.2$ .

### 2.3 Cloud Saturation and Bosenova Cycling

Superradiant growth drives the BH spin from its initial value toward the Regge trajectory  $a_* = a_*^{\text{crit}}$ , at which point the instability saturates. The fraction of BH mass transferred to the cloud at saturation is determined by simultaneous conservation of energy and angular momentum. For the dominant  $\{2, 1, 1\}$  state at  $\alpha \simeq 0.2$  and  $a_* \rightarrow 1$  this fraction is approximately 10.8% [32], consistent with our numerical calculation of 10.81% shown in Fig. 4. The corresponding saturation occupation number is

$$N_{\text{sat}} \approx \frac{0.1 M_{\text{BH}}}{\mu} \approx 10^{75} \left(\frac{M_{\text{BH}}}{10^{-5} M_{\odot}}\right) \left(\frac{10^{-6} \text{ eV}}{\mu}\right). \quad (2.13)$$

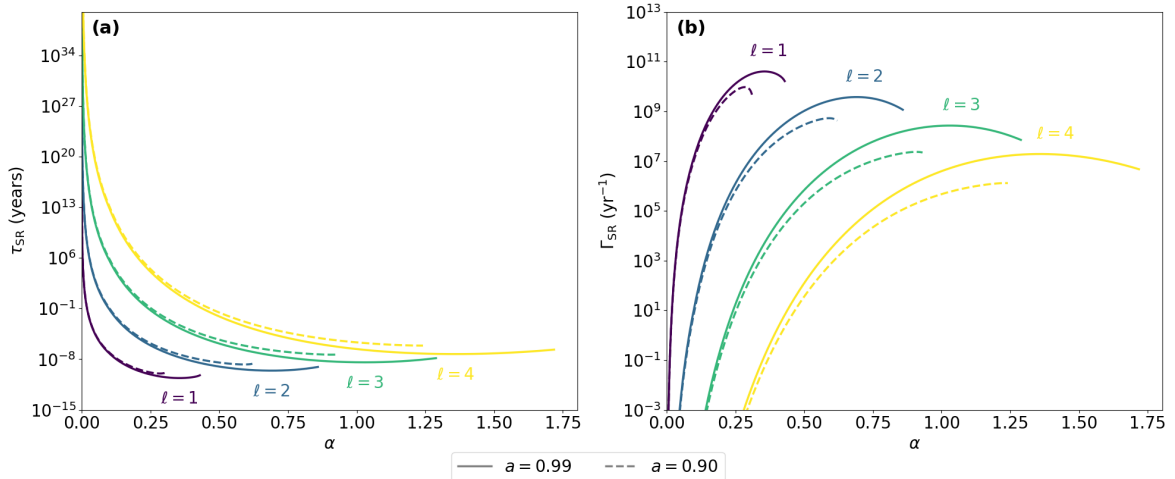


**Figure 2:** (a) Estimates of superradiance lifetime  $\tau = \Gamma^{-1}$  as a function of  $\alpha$  and azimuthal quantum number  $\ell = m$  for a  $10^{-6} M_{\odot}$  BH. Solid lines show  $a = 0.99$ , dashed lines show  $a = 0.90$ . (b) Superradiance rate  $\Gamma_{\text{SR}}$  as a function of  $\alpha$  for the same parameter space. Superradiance continues until  $m\Omega_{\text{H}} \geq \omega$  is violated through spin extraction via the superradiant cloud.

The enormous value of  $N_{\text{sat}}$ —a consequence of the tiny boson mass—is what enables the macroscopic, coherent GW emission discussed in subsequent sections.

For bosons with attractive self-interactions, parametrized by the axion decay constant  $f_a$ , a separate ceiling on the occupation number arises from the *bosenova* instability [16, 25]. When the occupation number exceeds

$$N_{\text{bosenova}} \approx 5 \times 10^{78} \frac{n^4}{\alpha^3} \left( \frac{M}{M_{\odot}} \right)^2 \left( \frac{f_a}{M_P} \right)^2, \quad (2.14)$$

attractive self-interactions overcome the gravitational binding energy and the cloud collapses [25, 26]. The implosion deposits most of the extracted angular momentum back into the BH in a burst lasting  $\sim r_g/c$ , after which superradiance restarts at reduced spin. This cycling behavior caps the effective occupation number at  $N_{\text{eff}} \equiv \min(N_{\text{sat}}, N_{\text{bosenova}})$ .

For QCD-axion values  $f_a \sim 10^{16}$  GeV we find  $f_a/M_P \sim 10^{-3}$ , giving

$$\frac{N_{\text{bosenova}}}{N_{\text{sat}}} \sim 5 \times 10^6 \left( \frac{n^4/\alpha^3}{10} \right) \left( \frac{M_{\text{BH}}}{10^{-5} M_{\odot}} \right) \left( \frac{\mu}{10^{-6} \text{ eV}} \right) \left( \frac{f_a/M_P}{10^{-3}} \right)^2, \quad (2.15)$$

so the bosenova threshold is not reached before saturation in the bulk of our PBH parameter space. We include  $N_{\text{bosenova}}$  as an upper bound in all strain calculations, but note that for QCD-axion-like couplings it is non-restrictive. For very small  $f_a$  (e.g., light moduli with  $f_a \ll M_P$ ) the bosenova may dominate and the cloud cycles; such scenarios, while physically interesting, fall outside the scope of this paper.

Finally, we note that accreting matter onto the BH can spin it back toward  $a_* = 1$ , potentially restarting superradiance after partial spin-down or counteracting the spin-down while the cloud is growing. For isolated PBHs in vacuum—the scenario relevant to the PBH mass range considered here—negligible accretion is expected and superradiance proceeds unimpeded. The visible imprint of accretion is the left-hand suppression of the allowed region

in Fig. 1: as  $M_{\text{BH}}$  decreases at fixed  $\mu$ , the condition  $\alpha < m/2$  becomes harder to satisfy if spin-up by accretion is competitive with superradiant spin-down. We treat this effect as absent in what follows.

### 3 Gravitational-Wave Signatures from Isolated Gravitational Atoms

Before examining the modifications introduced by a binary companion (Sec. 4), we establish the GW signals from an *isolated* gravitational atom (GA) as the baseline against which binary-induced effects will be compared. Two physically distinct emission channels are active once superradiance saturates:

1. *Level transitions* (Sec. 3.1), in which the gravitational self-interaction of two simultaneously occupied superradiant levels drives bosons from the higher to the lower state, emitting quasi-monochromatic GWs at the Bohr frequency  $\omega_{\text{tr}}$ .
2. *Boson annihilation* (Sec. 3.2), in which pairs of cloud bosons annihilate into a single graviton at  $\omega_{\text{ann}} \simeq 2\mu_a$ , producing an extremely long-lived, slowly decaying signal.

In both cases the signal is quasi-monochromatic and persists on timescales far exceeding the ring-up time  $\tau_{\text{ring}}$  of a resonant-cavity detector, satisfying the fundamental detectability prerequisite for ADMX-type experiments. The time-domain waveforms derived here serve as inputs to the frequency-domain strain templates of App. A.

Throughout this section we assume the BH spin has been reduced to the saturation value  $a_*^{\text{crit}}$  (Eq. (2.5)) and that the cloud is in a well-defined two-level configuration consisting of an “excited” state with quantum numbers  $(n_e, \ell, m)$  and a “ground” state  $(n_g, \ell, m)$ , with  $n_e > n_g$ . All cloud masses are computed numerically using the results of Refs. [35, 36], and superradiance rates use the relativistic calculations of Refs. [33, 34].

#### 3.1 Gravitational Waves from Level Transitions

##### 3.1.1 Two-level population dynamics

When the BH spin lies above the critical value for two levels simultaneously, both states are initially populated independently through superradiance. For occupation numbers well below saturation, where the gravitational self-interaction between levels is negligible, each level grows independently:

$$\frac{dN_g}{dt} = N_g \Gamma_{\text{SR}}^{(n_g)}, \quad (3.1)$$

$$\frac{dN_e}{dt} = N_e \Gamma_{\text{SR}}^{(n_e)}, \quad (3.2)$$

where  $\Gamma_{\text{SR}}^{(n)}$  is the superradiant instability rate for level  $n$  (Eq. (2.10)). The  $\{6, 4, 4\}$  and  $\{5, 4, 4\}$  states have nearly equal instability rates at the benchmark parameters of Fig. 3, so both grow on comparable timescales.

This picture changes once the occupation numbers become large enough that the gravitational self-interaction of the cloud is no longer negligible. A macroscopic cloud in state  $|n_e, \ell, m\rangle$  generates a time-dependent potential  $V_*(t, \mathbf{r})$  that mixes the two levels through

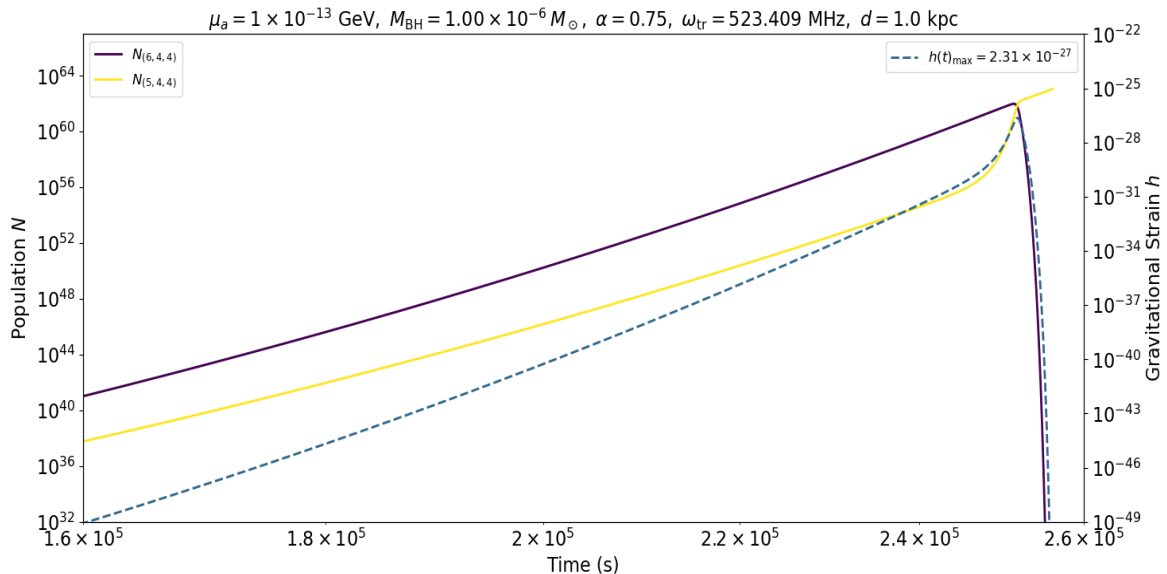


**Figure 3:** Time evolution of the occupation numbers  $N_{\{6,4,4\}}$  and  $N_{\{5,4,4\}}$  alongside the corresponding gravitational-wave strain envelope  $h(t)$  (dashed), computed for  $\mu_a = 10^{-4}$  eV,  $M_{\text{BH}} = 10^{-6} M_{\odot}$ ,  $\alpha = 0.75$ , and a source distance of  $d = 1$  kpc. At early times both states grow independently under superradiance (Eqs. (3.1)–(3.2)). Once  $N_e$  is large enough, the gravitational self-interaction coupling  $\Gamma_t N_g N_e$  (Eq. (3.5)) begins to dominate the excited-state dynamics, and a net flux of bosons cascades into the lower state, emitting a nearly monochromatic gravitational wave analogous to stimulated emission in atomic physics. The transition frequency  $\omega_{\text{tr}} = 526.4$  MHz lies within the ADMX scan band. The peak strain reflects a specific benchmark configuration and is not representative of the maximal transition strain, which can reach  $\sim 10^{-23}$  for more favorable parameters.

the matrix element  $\langle n_g, \ell, m | V_*(t, \mathbf{r}) | n_e, \ell, m \rangle$ . This introduces a coherent transition rate  $\Gamma_t$ , coupling the two occupation numbers:

$$\frac{dN_g}{dt} = N_g \Gamma_{\text{SR}}^{(n_g)} + N_g N_e \Gamma_t, \quad (3.3)$$

$$\frac{dN_e}{dt} = N_e \Gamma_{\text{SR}}^{(n_e)} - N_g N_e \Gamma_t. \quad (3.4)$$

The term  $-N_g N_e \Gamma_t$  acts as a stimulated-emission drain on the excited state: as  $N_e$  grows, the transition rate accelerates, depopulating  $|n_e\rangle$  and populating  $|n_g\rangle$  while emitting a GW at the Bohr frequency. The per-boson transition rate is obtained from the gravitational quadrupole formula applied to the off-diagonal current between the two levels [16, 17]:

$$\Gamma_t \sim \frac{2 G_N \omega_{\text{tr}}^5}{5} \mu_a^2 r_c^4 = \mathcal{O}(10^{-6} - 10^{-8}) \frac{G_N \alpha^9}{r_g^3}, \quad (3.5)$$

where  $\omega_{\text{tr}}$  is the transition frequency (Eq. (3.6)),  $r_c \sim n^2 r_g / \alpha^2$  is the characteristic cloud radius, and  $r_g = GM$  is the gravitational radius. The scaling  $\Gamma_t \propto \alpha^9 / r_g^3$  follows from substituting  $r_c^4 \propto r_g^4 / \alpha^8$  and  $\omega_{\text{tr}} \propto \mu_a \alpha^2 \propto \alpha^3 / r_g$  into the first form. The numerical range reflects the variation across quantum numbers  $n$  and  $\ell$  for the configurations of interest [16].

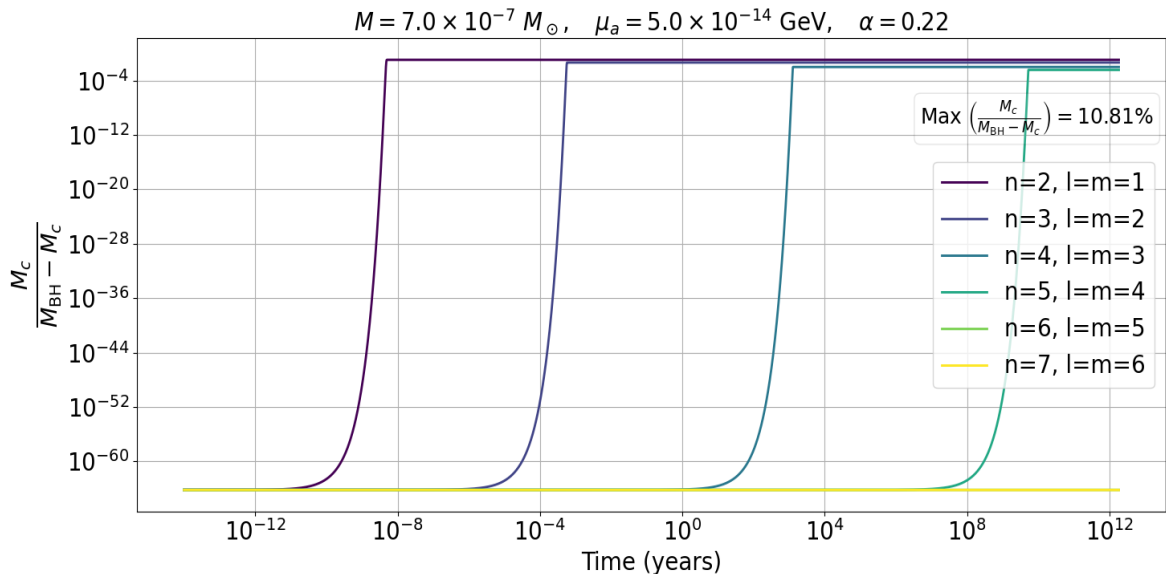


**Figure 4:** Fractional BH mass transferred to each superradiant level,  $M_c/(M_{\text{BH}} - M_c)$ , as a function of time for states with  $n = m + 1$ ,  $\ell = m$ , and  $m = 1\text{--}6$ , computed at  $M_{\text{BH}} = 6 \times 10^{-7} M_{\odot}$ ,  $\mu_a = 5 \times 10^{-5} \text{ eV}$ ,  $\alpha = 0.22$ . The  $\{2, 1, 1\}$  level (darkest) reaches its saturation first and at the largest fractional mass. The maximum extracted mass for the most efficient state is 10.81%, in excellent agreement with the analytic upper bound of 10.8% derived in Ref. [32] for  $\alpha \approx 0.2$  and  $a_* \rightarrow 1$ . Higher- $m$  levels saturate later and accumulate correspondingly smaller clouds, as their slower growth is overtaken by the already-saturated lower levels.

### 3.1.2 Time-domain gravitational-wave strain

The GW angular frequency for transitions between states  $(n_e, \ell, m)$  and  $(n_g, \ell, m)$  with  $n_e > n_g$  is the Bohr frequency:

$$\omega_{\text{tr}} = \omega_{n_g \ell m} - \omega_{n_e \ell m} \simeq \frac{\mu_a \alpha^2}{2} \left( \frac{1}{n_g^2} - \frac{1}{n_e^2} \right), \quad (3.6)$$

where we have used the leading-order hydrogenic approximation. For the  $\{6, 4, 4\} \rightarrow \{5, 4, 4\}$  transition at the benchmark parameters of Fig. 3, this gives  $f_{\text{tr}} = \omega_{\text{tr}}/(2\pi) \approx 526 \text{ MHz}$ .

The oscillating quadrupole moment of the two-level system sources a GW whose strain envelope is obtained from the quadrupole luminosity formula. Expressing the instantaneous radiated power as  $P_{\text{tr}} = G_N \omega_{\text{tr}}^2 |\dot{Q}_{\text{tr}}|^2/5$  and the resulting strain amplitude as  $h^2 \sim P_{\text{tr}}/(r^2 \omega_{\text{tr}}^2)$ , one finds [16, 17]:

$$h_{0,\text{tr}}(t) = \sqrt{\frac{4G_N}{r^2 \omega_{\text{tr}}} \Gamma_t N_g(t) N_e(t)}, \quad (3.7)$$

where  $N_g(t)$  and  $N_e(t)$  are solutions of Eqs. (3.3)–(3.4). This is the *slowly-varying envelope* of the GW signal: it evolves on timescales set by  $\Gamma_{\text{SR}}$  and  $\Gamma_t$ , which are much longer than the GW oscillation period  $2\pi/\omega_{\text{tr}}$ . The full waveform, decomposed into the standard plus and

cross polarizations, is:

$$h_+(t) = h_{0,\text{tr}}(t) \frac{1 + \cos^2 \iota}{2} \cos(\omega_{\text{tr}} t + \phi_0), \quad (3.8)$$

$$h_\times(t) = h_{0,\text{tr}}(t) \cos \iota \sin(\omega_{\text{tr}} t + \phi_0), \quad (3.9)$$

where  $\iota$  is the inclination of the BH spin axis with respect to the line of sight and  $\phi_0$  is an arbitrary initial phase. The signal is quasi-monochromatic at  $\omega_{\text{tr}}$  with a slowly drifting amplitude; it is the amplitude modulation through  $h_{0,\text{tr}}(t)$  that, in the frequency domain (App. A), produces the characteristic narrow Lorentzian lineshape at  $f = \omega_{\text{tr}}/2\pi$ .

### 3.1.3 Saturation occupation number and peak strain

The peak GW strain occurs at the moment when the coupled system (Eqs. (3.3)–(3.4)) transitions from the superradiance-dominated to the transition-dominated regime, i.e., when  $\Gamma_t N_e \sim \Gamma_{\text{SR}}^{(n_e)}$ . This equal population condition corresponds to the moment of maximum stimulated emission and thus maximum GW power. Substituting  $N_g \sim N_e \sim N_{\text{sat}}/2$  into Eq. (3.7) gives the peak strain:

$$h_{0,\text{tr}}^{\text{peak}} \simeq \frac{1}{2} \sqrt{\frac{4 G_N \Gamma_t N_{\text{sat}}^2}{r^2 \omega_{\text{tr}}}} \simeq 10^{-23} \left( \frac{1 \text{ kpc}}{r} \right) \left( \frac{\alpha}{0.3} \right)^{9/2} \left( \frac{M}{10^{-7} M_\odot} \right)^{3/2}, \quad (3.10)$$

where the numerical scaling absorbs  $G_N$ ,  $r_g$ , and  $N_{\text{sat}}(\alpha, M)$ . Here the numerical estimate corresponds to near-optimal choices of  $\alpha$  and level structure; less favorable configurations can yield substantially smaller peak strains. Using the benchmark parameters of  $M = 10^{-6} M_\odot$  and  $\alpha = 0.75$  we obtain an  $N_{\text{sat}} \approx 10^{62}$ . This scaling corresponds to optimal transition configurations. The significantly smaller value  $h_{\text{max}} \approx 10^{-27}$  at 1 kpc seen in Fig. 3 reflects the specific benchmark choice adopted there, rather than the maximal achievable transition strain.

### 3.1.4 Signal lifetime

Once the transition-dominated phase begins, the excited state drains with a characteristic timescale

$$\tau_{\text{tr}} \sim \frac{1}{\Gamma_t N_{\text{sat}}} \sim \mathcal{O}(10^3\text{--}10^6) \text{ yr}, \quad (3.11)$$

for the parameters relevant to MHz–GHz emission. Since  $\tau_{\text{tr}} \gg \tau_{\text{ring}} \sim 1/\Delta f_{\text{band}} \sim 10^{-5}$  s (for a cavity bandwidth  $\Delta f_{\text{band}} \sim 10$  kHz), the level-transition signal is effectively continuous on detector timescales. The extremely narrow spectral width  $\Delta f \sim \tau_{\text{tr}}^{-1}/(2\pi) \ll 1$  Hz (compared to the carrier frequency  $f_{\text{tr}} \sim$  MHz–GHz) makes this signal highly coherent over any realistic observation window; the resulting frequency-domain Lorentzian template is developed in App. A.

## 3.2 Gravitational Waves from Boson Annihilation

### 3.2.1 Annihilation frequency and rate

When two cloud bosons annihilate they produce a single graviton. Each boson in the bound state has energy  $\omega_b = \omega_{n\ell m}$ , so the emitted graviton carries

$$\omega_{\text{ann}} = 2\omega_{n\ell m} \simeq 2\mu_a \left( 1 - \frac{\alpha^2}{2n^2} \right), \quad (3.12)$$

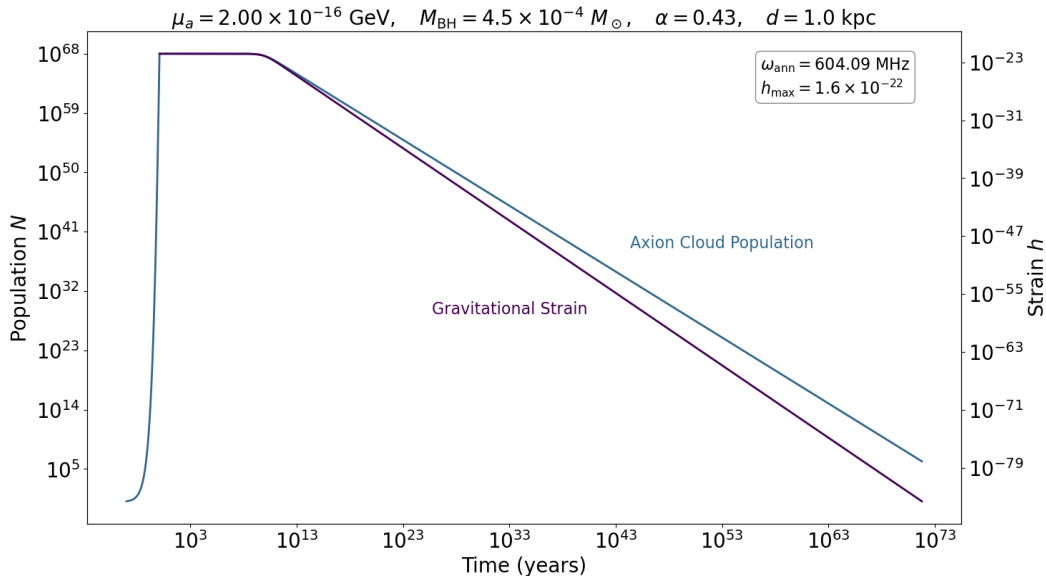


**Figure 5:** Time evolution of the cloud occupation number  $N(t)$  (solid) and the corresponding annihilation strain envelope  $h_{0,\text{ann}}(t)$  (dashed), computed for  $\mu_a = 2 \times 10^{-7}$  eV,  $M_{\text{BH}} = 4.5 \times 10^{-4} M_{\odot}$ ,  $\alpha = 0.43$ , and  $d = 1$  kpc. The occupation number grows during the superradiant phase (left portion of the curve) until it saturates at  $N_{\text{max}}$ , after which  $N(t)$  decays as  $[1 + \Gamma_a N_{\text{max}} t]^{-1}$  (Eq. (3.14)) as boson pairs annihilate into gravitons. The corresponding strain peaks at  $h_{0,\text{ann}}^{\text{max}} \approx 10^{-22}$  and decays on a timescale  $\tau_{\text{ann}} = (\Gamma_a N_{\text{max}})^{-1}$  that can exceed the Hubble time, making the signal effectively monochromatic and persistent for any observation campaign. The annihilation frequency  $\omega_{\text{ann}}/(2\pi) \approx 96$  MHz is within the ADMX scan band.

to leading order in  $\alpha$ . The  $\mathcal{O}(\alpha^2)$  correction shifts the emission frequency slightly below  $2\mu_a$ ; for the benchmark parameters of Fig. 5 this gives  $f_{\text{ann}} = \omega_{\text{ann}}/(2\pi) \approx 96.2$  MHz.

The pair-annihilation rate per boson—the rate at which a single pair converts into a graviton—is obtained from the gravitational quadrupole formula applied to the  $2\mu_a$  oscillation of the cloud’s stress–energy tensor [17]:

$$\Gamma_a \simeq C_{nlm} \left( \frac{\alpha/\ell}{0.5} \right)^{4\ell+4} \frac{G_N}{r_g^3}, \quad (3.13)$$

where the exponent  $p \equiv 4\ell+4$  is determined by the power of  $\alpha$  in the hydrogenic wavefunction overlap, and  $C_{nlm} \approx 10^{-10}$  is a dimensionless coefficient that depends weakly on  $n$  for  $n \lesssim \ell + 2$  [15, 17]. Concretely: for the lowest superradiant level  $\ell = m = 1$ , one has  $p = 8$ ; for  $\ell = m = 2$ ,  $p = 12$ ; and so on. Since  $\Gamma_a \propto \alpha^{4\ell+4}/r_g^3$  while  $\Gamma_{\text{SR}} \propto \alpha^{4\ell+5}/r_g$  and  $\Gamma_t \propto \alpha^9/r_g^3$ , the hierarchy  $\Gamma_{\text{SR}} \gg \Gamma_t \gg \Gamma_a$  holds over the entire parameter space of interest, confirming that annihilation is the slowest of the three processes.

### 3.2.2 Time-domain occupation number and strain

After superradiance saturates the cloud at  $N_{\text{max}}$  and the level-transition phase has depleted the excited state, the occupation number of the surviving ground level evolves under pure

annihilation. Solving  $dN/dt = -\Gamma_a N^2$  gives:

$$N(t) = \frac{N_{\max}}{1 + \Gamma_a N_{\max} t}, \quad (3.14)$$

starting from  $t = 0$  at saturation. The GW strain envelope follows directly from the quadrupole luminosity:

$$h_{0,\text{ann}}(t) = N(t) \sqrt{\frac{4 G_N}{r^2 \omega_{\text{ann}}}} \Gamma_a = \frac{N_{\max}}{1 + \Gamma_a N_{\max} t} \sqrt{\frac{4 G_N \Gamma_a}{r^2 \omega_{\text{ann}}}}, \quad (3.15)$$

which is the slowly-varying amplitude of the wave [17]. The full waveform polarizations are:

$$h_+(t) = h_{0,\text{ann}}(t) \frac{1 + \cos^2 \iota}{2} \cos(\omega_{\text{ann}} t + \phi_0), \quad (3.16)$$

$$h_\times(t) = h_{0,\text{ann}}(t) \cos \iota \sin(\omega_{\text{ann}} t + \phi_0), \quad (3.17)$$

where the inclination  $\iota$  and phase  $\phi_0$  carry the same meaning as in Eqs. (3.8)–(3.9). The envelope  $h_{0,\text{ann}}(t)$  includes the effects of BH mass and spin loss, which cause  $N_{\max}$  and  $\omega_{\text{ann}}$  to decrease slowly over time; these corrections are numerically small ( $\lesssim 10\%$  over cosmic timescales for the configurations considered) and are incorporated in our numerical calculations.

### 3.2.3 Peak strain scaling

The peak strain, attained at  $t = 0$  (saturation), is:

$$h_{0,\text{ann}}^{\text{peak}} = N_{\max} \sqrt{\frac{4 G_N \Gamma_a}{r^2 \omega_{\text{ann}}}} \simeq 10^{-22} \left( \frac{1 \text{ kpc}}{r} \right) \left( \frac{\alpha/\ell}{0.5} \right)^{2\ell+5/2} \left( \frac{M}{10^{-4} M_\odot} \right), \quad (3.18)$$

where the numerical scaling uses  $N_{\max} \sim M^2 (\tilde{a}_*^{\text{init}} - a_*^{\text{crit}}) \cdot \omega_{nlm}/m$  and the  $\Gamma_a$  scaling of Eq. (3.13). The normalization mass  $10^{-4} M_\odot$  corresponds to a PBH whose  $\ell = 1$  annihilation frequency lies near 100 MHz. For the benchmark parameters of Fig. 5, the simulated peak is  $h_{0,\text{ann}}^{\text{max}} \approx 10^{-22}$ , consistent with this estimate.

### 3.2.4 Signal lifetime and detectability window

The characteristic decay time of the annihilation signal is:

$$\tau_{\text{ann}} \equiv \frac{1}{\Gamma_a N_{\max}} \sim \frac{r_g^3}{G_N C_{nlm}} \left( \frac{0.5}{\alpha/\ell} \right)^{4\ell+4} \frac{1}{N_{\max}}, \quad (3.19)$$

which, for the parameters relevant to MHz–GHz emission, evaluates to  $\tau_{\text{ann}} \sim 10^{25}–10^{60}$  yr. This vastly exceeds both the Hubble time and any conceivable observation period, confirming that the annihilation signal is effectively a *monochromatic steady source* for the purposes of detection. The extremely slow decay also means that  $N(t) \approx N_{\max}$  throughout any observation, so  $h_{0,\text{ann}}$  is well approximated by its peak value.

Like the transition signal, the annihilation signal is continuous on detector timescales ( $\tau_{\text{ann}} \gg \tau_{\text{ring}}$ ), and its spectral width  $\Delta f \sim \tau_{\text{ann}}^{-1}/(2\pi) \lesssim 10^{-33}$  Hz is extraordinarily narrow. The frequency-domain template, detailed in App. A, takes the form of an exponential-integral function peaked at  $f_{\text{ann}} = \omega_{\text{ann}}/(2\pi)$  with a width set by  $\Gamma_a N_{\max}$ .

Property	Level transition	Annihilation
Emission frequency	$\omega_{\text{tr}}/(2\pi)$ , Eq. (3.6)	$\omega_{\text{ann}}/(2\pi)$ , Eq. (3.12)
Rate controlling amplitude	$\Gamma_t$ , Eq. (3.5)	$\Gamma_a$ , Eq. (3.13)
Peak strain at 1 kpc	$\sim 10^{-23}$	$\sim 10^{-22}$
Signal lifetime	$\tau_{\text{tr}} \sim 10^3\text{--}10^6$ yr, Eq. (3.11)	$\tau_{\text{ann}} \sim 10^{25}\text{--}10^{60}$ yr, Eq. (3.19)
Spectral width $\Delta f$	$\sim \tau_{\text{tr}}^{-1}/(2\pi) \ll 1$ Hz	$\lesssim 10^{-33}$ Hz
$\Delta f/f$	$\ll 10^{-6}$	$\ll 10^{-30}$
Signal type	Quasi-monochromatic transient	Persistent monochromatic

**Table 2:** Comparison of the two isolated-GA gravitational-wave channels for the PBH benchmark parameters of Table 1. Both signals satisfy  $\tau \gg \tau_{\text{ring}}$  and are therefore candidates for resonant-cavity detection in the MHz–GHz band. The level-transition signal is stronger at early times but decays over  $\tau_{\text{tr}}$ ; the annihilation signal is weaker but essentially eternal.

### 3.3 Summary and comparison of isolated-GA signals

Table 2 collects the key properties of the two isolated-GA GW channels for the benchmark parameter sets introduced in Table 1. The level-transition and annihilation signals differ in amplitude, duration, and spectral width, but share the property that both persist for times enormously exceeding the ring-up time of any resonant-cavity detector. This motivates the use of characteristic strain  $h_c(f) = 2f|\tilde{h}(f)|$  as the figure of merit (App. A), since the large number of coherent cycles accumulated over  $\tau_{\text{tr}}$  or  $\tau_{\text{ann}}$  enhances the characteristic strain above the raw amplitude by a factor  $\sqrt{f\tau}$ .

The key conclusion of this section is that *both* isolated-GA emission channels produce continuous, narrowband GWs in the MHz–GHz band for PBH masses in the range  $M_{\text{BH}} \sim 10^{-16}\text{--}10^{-4} M_{\odot}$ . Their detectability at a specific detector depends on the signal duration relative to  $\tau_{\text{ring}}$  (which is easily satisfied) and on whether the peak strain exceeds the detector noise floor.

## 4 Gravitational-Wave Signatures from Gravitational Atoms in Binaries

The emission channels studied in Sec. 3 treat the gravitational atom (GA) as evolving in isolation. In realistic astrophysical environments, however, a GA may reside in a binary system whose companion’s tidal field drives resonant transitions between cloud levels. When the orbital frequency  $\Omega_0$  sweeps through a Bohr frequency of the gravitational atom, the system behaves as a driven two-level quantum system and can undergo a Landau–Zener resonance [27, 28]. In this section we apply the binary-perturbation formalism of Kyriazis & Yang [29] to PBH binaries in natural units  $c = \hbar = 1$ , compute the characteristic GW strain of the transient burst produced by the resonant  $\{2, 1, 1\} \rightarrow \{2, 1, -1\}$  hyperfine transition, and assess the prospects for detection with ADMX.

#### 4.1 Time- and Frequency-Domain Waveforms

The gravitational-wave strain produced by tidal perturbations of a GA cloud from its binary companion can be expressed as [29]

$$h_{+,211}(t) = h_0 \frac{1 + \cos^2 \iota}{2} \operatorname{Re} \left[ e^{-2i\Delta m \varphi(t_{\text{re}})} Q(t_{\text{re}}) \right], \quad (4.1)$$

$$h_{\times,211}(t) = h_0 \cos \iota \operatorname{Im} \left[ e^{-2i\Delta m \varphi(t_{\text{re}})} Q(t_{\text{re}}) \right], \quad (4.2)$$

where  $\iota$  is the inclination angle between the line of sight and the normal to the binary orbital plane, and  $t_{\text{re}}$  is the retarded time. The binary orbital phase is  $\varphi(t) = \Omega_0 t + \frac{1}{2}\gamma t^2$ , which assumes a linearly chirping orbit with rate  $\dot{\Omega} = \gamma$  (see Eq. (4.6) below). The quantity  $\Delta m \equiv m_f - m_i = -2$  is the difference in azimuthal quantum numbers between the final ( $m_f = -1$ ) and initial ( $m_i = +1$ ) states of the  $\{2, 1, 1\} \rightarrow \{2, 1, -1\}$  transition. The complex modulation  $Q(t)$  captures the dynamics of the level population transfer: it encodes the evolving occupation-number amplitudes of the two mixed states as the binary sweeps through resonance, and its derivation and explicit form are given in Ref. [29]. The exponential factor  $e^{-2i\Delta m \varphi}$  carries the fast orbital-phase oscillation, while the variation of  $Q(t)$  is slow compared to  $1/\Omega_0$ .

The overall GW amplitude is set by

$$h_0 = \frac{24 q_c GM}{r} \frac{(GM\Omega_0)^2}{\alpha^4}, \quad (4.3)$$

where  $M$  is the mass of the host BH (the primary of the gravitational-atom–binary, or GAB, system),  $\Omega_0$  is the binary orbital frequency at resonance,  $r$  is the observer distance, and  $q_c \equiv M_{\text{cloud}}/M$  is the cloud-to-BH mass ratio. The latter is determined by the saturation condition [29]:

$$q_c = \frac{8\alpha^2 \left(1 - \frac{\alpha a_*}{m}\right)}{m^2 \left(1 - \sqrt{1 - \left(\frac{4\alpha}{m} \left(1 - \frac{\alpha a_*}{m}\right)\right)^2}\right)} - 1, \quad (4.4)$$

where  $m$  is the azimuthal quantum number of the initial state and  $a_*$  is the dimensionless BH spin. Throughout we set  $a_* = a_*^{\text{crit}}(m_i)$  (Eq. (2.5)), i.e., the spin is taken at the Regge-trajectory saturation value that maximizes  $\alpha$  for fixed boson mass.

For the rest of the section, we shall only concern ourselves with the “plus” polarization  $h_+$ , as the two strain polarizations only differ by a relative phase and inclination weight, which can be observed through the comparison between Eq. (4.1) and Eq. (4.2) for the time domain, and proved within Section A.3 for the frequency domain.

In frequency space, the Fourier transform of  $h_+(t)$  takes the analytic form [29]

$$\tilde{h}_+(f) = h_0 (1 + \cos^2 \iota) \sqrt{\pi} |\Delta m|^2 i e^{i\Psi_+(f)} \frac{\sqrt{z}}{|\Gamma| - i\pi(f - f_c)} e^{-\pi z} \exp \left[ -2z \arctan \left( \frac{\pi(f - f_c)}{|\Gamma|} \right) \right] \quad (4.5)$$

where  $f_c = \Omega_0/\pi$  is the carrier frequency (twice the orbital frequency divided by  $2\pi$ ), and the GW phase is  $\Psi_+(f) = fr + (f - f_c)^2/(4|\Delta m|\gamma) - \pi/4$ . The quantity  $\Gamma \equiv \Gamma_{\text{SR}}^{(2,1,-1)}$  is the superradiant instability rate of the *final* state  $\{2, 1, -1\}$  (Eq. (2.10)), which governs how rapidly bosons that have transitioned into  $m = -1$  fall back into the BH; it sets the spectral

width of the signal. Equation (4.5) describes a Lorentzian-shaped frequency-domain burst centered at the peak frequency  $f_p$  (Eq. (4.9)), with width  $\sim |\Gamma|/\pi$ .

The orbital chirp rate, derived from the leading-order gravitational-wave energy loss of a circular binary with mass ratio  $q \equiv M_c/M$ , is

$$\frac{\gamma}{\Omega_0^2} = \frac{96}{5} \frac{q}{(1+q)^{1/3}} (GM\Omega_0)^{5/3}. \quad (4.6)$$

The adiabaticity parameter  $z$  governs the degree of population transfer during the resonance. It is defined as

$$z \equiv \frac{\eta^2}{|\Delta m| \gamma}, \quad (4.7)$$

where  $\eta = \langle \psi_f | V_*(t, \mathbf{r}) | \psi_i \rangle$  is the tidal mixing amplitude between the  $\{2, 1, 1\}$  and  $\{2, 1, -1\}$  states evaluated numerically from the companion's gravitational potential  $V_*$ . In the limit  $z \ll 1$  the resonance is non-adiabatic: the orbital frequency sweeps through the Bohr frequency too rapidly for the levels to equilibrate, and only a fraction  $\sim z$  of the cloud population is transferred. In the opposite limit  $z \gg 1$  the resonance is adiabatic and the populations invert almost completely. In practice, however, the final state  $\{2, 1, -1\}$  has a non-zero instability rate  $|\Gamma|$  that continuously drains bosons back into the BH, effectively truncating the transition and limiting the maximum transferred population regardless of  $z$ . This instability is fully accounted for in Eq. (4.5)

As the binary sweeps through the resonance band, the GW signal duration is

$$\Delta t = \frac{2|\Gamma|}{\gamma} (1 + 2z). \quad (4.8)$$

The peak GW frequency is shifted from the carrier by the finite- $z$  correction,

$$f_p = f_c - \frac{2z|\Gamma|}{\pi} = \frac{\Omega_0}{\pi} - \frac{2z|\Gamma|}{\pi}. \quad (4.9)$$

For  $z \ll 1$  the peak frequency approaches the orbital carrier,  $f_p \rightarrow f_c$ ; for  $z \gg 1$  the signal is redshifted from the carrier by a term proportional to  $|\Gamma|$ , quantifying the downward pull of the final-state decay.

## 4.2 Parameter Space Constraints

Several physical requirements simultaneously constrain the allowed  $(\alpha, q)$  parameter space. The binary orbit is treated in the linear-chirp approximation (Eq. (4.6)), which is valid only when the fractional frequency change during the resonance is small:  $\Delta\Omega/\Omega_0 = \gamma \Delta t/\Omega_0 \ll 1$ . The annihilation timescale of the initial  $\{2, 1, 1\}$  state (Eq. (3.19)) must also exceed the resonance crossing time  $\Delta t$ , otherwise the cloud is depleted by annihilation before it can undergo the binary-driven transition. In practice, both of these are less restrictive than the most stringent condition, which requires the signal duration to be shorter than the binary merger timescale:

$$\Delta t < t_{\text{merge}}, \quad (4.10)$$

where the Peters-formula merger time at orbital frequency  $\Omega_0$  is

$$t_{\text{merge}} = \frac{5}{256} G^{-5/3} \frac{M}{(M\Omega_0)^{8/3}} \frac{(1+q)^{1/3}}{q}. \quad (4.11)$$

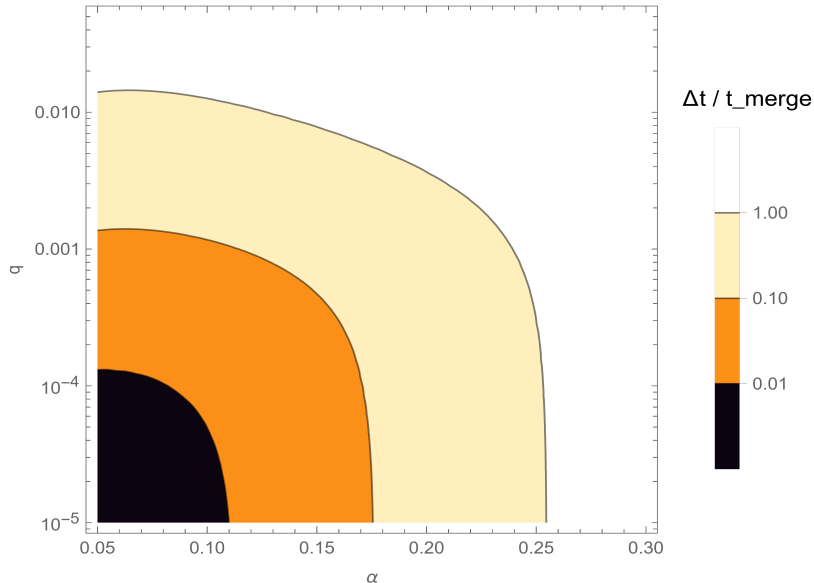


**Figure 6:** Ratio  $\Delta t/t_{\text{merge}}$  (Eqs. (4.8) and (4.11)) in the  $(\alpha, q)$  parameter plane for the  $\{2, 1, 1\} \rightarrow \{2, 1, -1\}$  transition, evaluated at the resonant orbital frequency  $\Omega_0$ . Contours correspond to  $\Delta t/t_{\text{merge}} = 0.01$  (inner), 0.1 (middle), and 1 (outer). The white region, where  $\Delta t/t_{\text{merge}} > 1$ , is excluded: the signal duration would exceed the remaining merger time, violating the linear-orbit approximation, and the binary would not be intact. The allowed region is bounded by  $\alpha \lesssim 0.26$  and  $q \lesssim 0.01$ ; throughout Secs. 4.3 and 5 we adopt the benchmark values  $\alpha = 0.21$  and  $q = 10^{-3}$ , which lie well within this allowed region.

The condition (4.10) ensures that the resonant transition occurs while the binary is still intact—a prerequisite for the waveform model of Sec. 4.1 to apply.

Figure 6 displays the ratio  $\Delta t/t_{\text{merge}}$  in the  $(\alpha, q)$  plane, with contours at  $\Delta t/t_{\text{merge}} = 0.01, 0.1, 1$ . The region ( $\Delta t/t_{\text{merge}} > 1$ ) is excluded because the transition would not complete before merger. The figure shows that the allowed region is bounded by  $\alpha \lesssim 0.26$  and  $q \lesssim 0.01$ . We enforce these constraints in all subsequent calculations in this section.

### 4.3 Detectability Prospects for PBH Gravitational-Atom Binaries

We now apply the binary-perturbation formalism to PBH systems and assess detectability at ADMX. To avoid overestimating the signal we adopt conservative numerical inputs throughout: (i) relativistic instability rates from Refs. [33, 34] for the final-state decay rate  $\Gamma$ , rather than the leading-order analytic approximation of Eq. (2.10); (ii) numerically computed mixing amplitudes  $\eta = \langle \psi_f | V_*(t, \mathbf{r}) | \psi_i \rangle$ ; and (iii) numerically computed cloud masses  $M_{\text{cloud}}$  from Refs. [35, 36].

#### 4.3.1 Peak-frequency map in the PBH mass range

Figure 7 shows the peak GW frequency  $f_p$  (Eq. (4.9)) across the  $M_{\text{BH}}-\alpha$  parameter space for several values of the boson mass  $\mu_b$ , with the companion-to-host mass ratio fixed at  $q = 10^{-3}$ . We restrict to the PBH mass range  $M_{\text{BH}} \in [10^{-16}, 10^1 M_\odot]$  and exclude parameter combinations outside the allowed region of Fig. 6. For the hyperfine transition  $\{2, 1, 1\} \rightarrow$

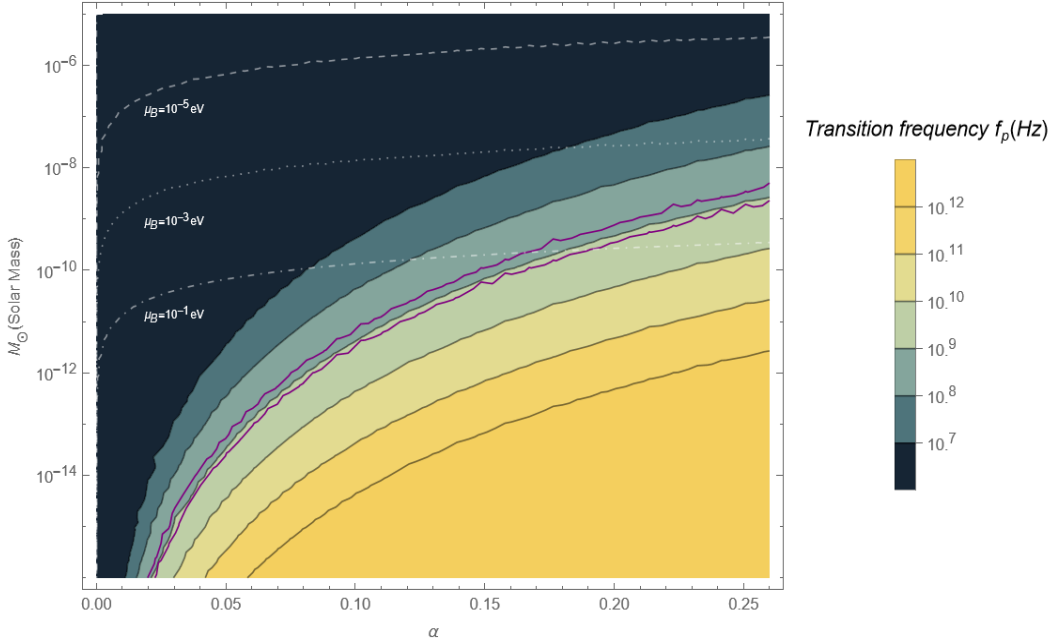


**Figure 7:** Peak transition frequency  $f_p$  (Eq. (4.9)) in the  $M_{\text{BH}}-\alpha$  parameter space for the  $\{2, 1, 1\} \rightarrow \{2, 1, -1\}$  hyperfine transition, for boson masses  $\mu_b = 10^{-5}$  eV (top),  $10^{-3}$  eV (middle), and  $10^{-1}$  eV (bottom), with  $q = 10^{-3}$  fixed. The PBH mass range cropped to  $M_{\text{BH}} \in [10^{-16}, 10^{-5} M_{\odot}]$  is shown, corresponding to the HF-band. The ADMX Run-1 scan band (0.645–1.4 GHz) is highlighted in purple; it is accessible for  $M_{\text{BH}} \sim 10^{-9}$ – $10^{-10} M_{\odot}$  and  $\mu_b \sim 10^{-1}$  eV at  $\alpha \sim 0.2$ . Sources lying in this band are the primary targets of the detectability analysis in Sec. 4.3.

$\{2, 1, -1\}$ , the superradiance condition  $\alpha < m/2 = 0.5$  is automatically satisfied within the constrained region.

The figure demonstrates that GW signals from binary-perturbed GA systems naturally populate the ultra-high-frequency (UHF) band—including the GHz range targeted by ADMX—if and only if the host BH is of primordial origin. The ADMX Run-1 frequency scan range (0.645–1.4 GHz, shown in purple) is intersected by trajectories with  $M_{\text{BH}} \sim 10^{-9}$ – $10^{-10} M_{\odot}$  and  $\mu_b \sim 10^{-1}$  eV at  $\alpha \sim 0.2$ , in direct agreement with the GW frequency map established in Sec. 2.

#### 4.3.2 Benchmark waveform and ring-up criterion

Figure 8 shows the time-domain strain  $h_+(t)$  and its Fourier transform  $\tilde{h}(f)$  for the benchmark binary GA system with

$$\alpha = 0.21, \quad M = 6 \times 10^{-10} M_{\odot}, \quad q = 10^{-3}, \quad r = 10 \text{ kpc}. \quad (4.12)$$

These parameters lie within the allowed region of Fig. 6, place the peak frequency  $f_p = 1.07$  GHz within the ADMX band, and correspond to the event rates computed in Sec. 5. The resulting signal is a quasi-monochromatic, transient GW burst.

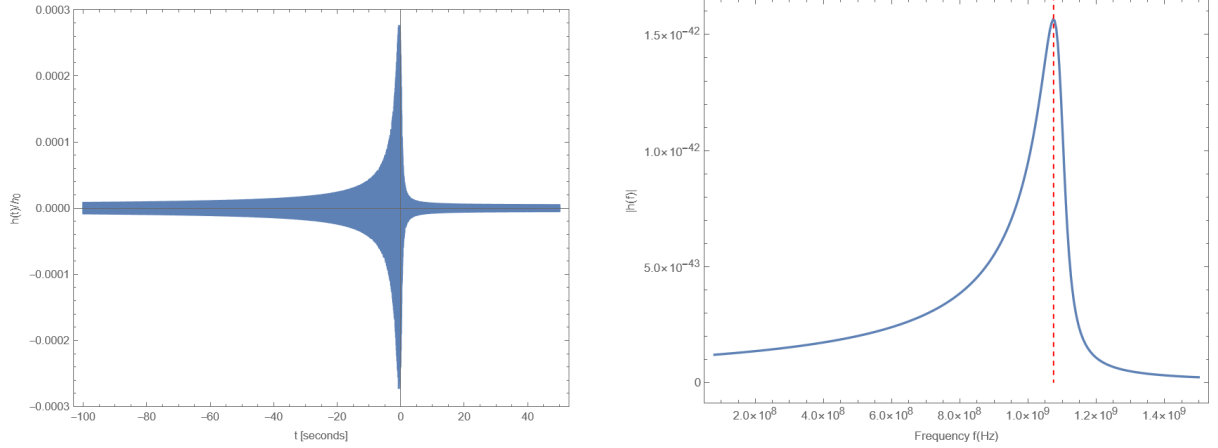


**Figure 8:** Time-domain strain  $h_+(t)$  (left) and frequency-domain amplitude  $|\tilde{h}(f)|$  (right) for the benchmark binary GA system of Eq. (4.12):  $\alpha = 0.21$ ,  $M = 6 \times 10^{-10} M_\odot$ ,  $q = 10^{-3}$ ,  $r = 10$  kpc. In the time domain the signal is a short quasi-monochromatic burst with duration  $\Delta t$  (Eq. (4.8)). In the frequency domain the signal is a Lorentzian-shaped peak centered at the peak frequency  $f_p = 1.07$  GHz (red dashed line), with spectral width  $\sim |\Gamma|/\pi$ . Both panels are computed using Eqs. (4.1) and (4.5) with the numerical inputs described in Sec. 4.3.

For resonant-cavity detectors such as ADMX, a signal is detectable only if the duration of the GW burst within the cavity bandwidth satisfies

$$\Delta t \gtrsim \tau_{\text{ring}} \equiv \frac{1}{\Delta f_{\text{band}}}, \quad (4.13)$$

where  $\Delta f_{\text{band}} \simeq f/Q$  is the cavity bandwidth and  $\tau_{\text{ring}}$  is the ring-up time required for the cavity to accumulate a detectable signal. For ADMX at  $f \sim 1$  GHz and  $Q \sim 8 \times 10^4$ , one has  $\tau_{\text{ring}} \sim 80 \mu\text{s}$ . We verify that  $\Delta t > \tau_{\text{ring}}$  across the *entire*  $M_{\text{BH}}-\alpha$  parameter space for  $q = 10^{-3}$ , regardless of the resonant frequency. The ring-up condition is therefore not the binding constraint; as shown in the next subsection, it is the signal strain that falls critically short.

### 4.3.3 ADMX sensitivity comparison

The minimum GW strain detectable by a resonant cavity is [1]

$$h_{\text{min}} = 3 \times 10^{-22} \left( \frac{0.1}{\eta_n} \right) \left( \frac{8 \text{ T}}{|\mathbf{B}|} \right) \left( \frac{0.1 \text{ m}^3}{V_{\text{cav}}} \right)^{5/6} \left( \frac{10^5}{Q} \right)^{1/2} \times \left( \frac{T_{\text{sys}}}{1 \text{ K}} \right)^{1/2} \left( \frac{1 \text{ GHz}}{f} \right)^{3/2} \left( \frac{\Delta f}{10 \text{ kHz}} \right)^{1/4} \left( \frac{1 \text{ min}}{\Delta t} \right)^{1/4}, \quad (4.14)$$

where  $\eta_n$  is the cavity–GW coupling coefficient,  $|\mathbf{B}|$  is the axial magnetic field,  $V_{\text{cav}}$  is the cavity volume,  $Q$  is the quality factor,  $T_{\text{sys}}$  is the system noise temperature,  $f$  the resonant frequency, and  $\Delta f \simeq f/Q$  the cavity bandwidth. For ADMX Run 1 the relevant parameters are  $\eta_n \sim 0.1$ ,  $|\mathbf{B}| = 0.75$  T,  $V_{\text{cav}} = 136$  L,  $Q \sim 8 \times 10^4$ ,  $T_{\text{sys}} = 0.6$  K, and  $f \in [0.65, 1.4]$  GHz [1], giving a typical threshold  $h_{\text{min}} \sim 10^{-22}$  within the ADMX band. The GW characteristic strain for binary-induced transitions is  $h_c(f) = 2f|\tilde{h}(f)|$  with  $\tilde{h}(f)$  given by Eq. (4.5), Fig. 13 shows the characteristic strain for the benchmark parameters of Eq. (4.12).

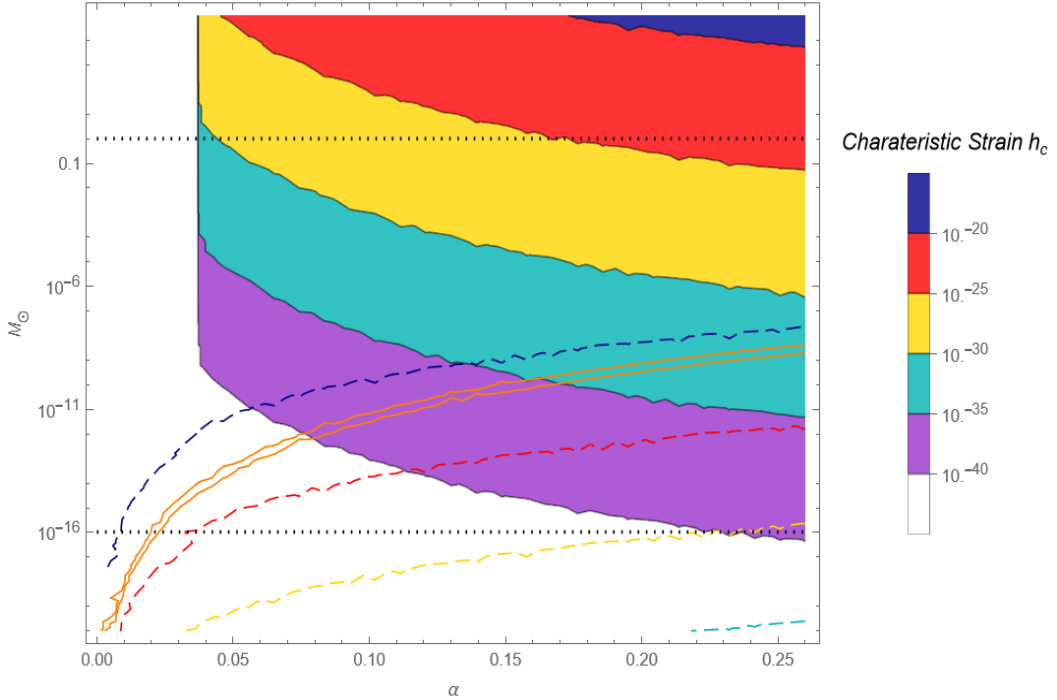


**Figure 9:** GW characteristic strain  $h_c$  (filled contours) and ADMX minimum detectable strain  $h_{\min}$  (dashed contours, Eq. (4.14)) for binary GA systems in the  $M_{\text{BH}}-\alpha$  plane, with  $q = 10^{-3}$  and  $r = 10$  kpc. Filled contour levels span  $h_c \in [10^{-40}, 10^{-20}]$ ; dashed contour levels show the same decades of  $h_{\min}$ , computed without restricting  $f$  to the ADMX hardware band. The orange solid curves overlay the ADMX frequency-band boundaries from Fig. 7, delimiting the region where ADMX can physically respond; within this region  $h_{\min} \sim 10^{-22}$ . The PBH mass range  $10^{-16} M_{\odot} \lesssim M_{\text{PBH}} \lesssim 1 M_{\odot}$  is bounded by the black dotted lines. No  $h_c$  contour overlaps a  $h_{\min}$  contour of equal magnitude within the PBH mass range at this distance, demonstrating that the signal falls orders of magnitude below the ADMX detection threshold.

Figure 9 displays both  $h_c$  (filled contours) and  $h_{\min}$  (dashed curves) across the  $M_{\text{BH}}-\alpha$  plane at  $q = 10^{-3}$  and  $r = 10$  kpc. The dashed contours of  $h_{\min}$  are evaluated at fixed values of the ADMX sensitivity parameter (Eq. (4.14)) but without restricting  $f$  to the ADMX hardware band; the orange solid curves then overlay the ADMX frequency range from Fig. 7 to delineate the region where the ADMX hardware could physically respond, during Run1 data, in turn corresponding to  $h_{\min} \sim 10^{-22}$ . The PBH mass range of primary interest,  $10^{-16} M_{\odot} \lesssim M_{\text{PBH}} \lesssim 1 M_{\odot}$ , is bounded by the black dotted lines.

For the benchmark parameters at  $r = 10$  kpc, the characteristic strain  $h_c$  falls *several orders of magnitude* below the ADMX detection threshold throughout the accessible parameter space. No overlap between the  $h_c$  and  $h_{\min}$  contours of equal magnitude is found within the PBH mass range, confirming that ADMX as currently configured cannot detect the binary-induced burst at astrophysically motivated distances.

The gap between  $h_c$  and the ADMX threshold persists even when one optimizes over the remaining free parameters. Increasing the mass ratio  $q$  toward its upper bound  $q \lesssim 0.01$

(Sec. 4.2) enhances  $h_c$  only modestly, with the most direct path to improved sensitivity is reducing the source distance  $r$ : from Eq. (4.3),  $h_0 \propto 1/r$ , so ADMX threshold strains are reached only at  $r \lesssim 1$  AU. Such distances are strongly disfavored by merger-rate arguments, as we demonstrate quantitatively in Sec. 5.

#### 4.4 Doppler Frequency Shift for Solar-System Flybys

The only scenario in which a PBH binary could approach within  $\sim 1$  AU is a transient flyby through the solar system. In this case the relative velocity between Earth and the binary imprints a Doppler shift on the observed GW frequency. We estimate the maximum frequency shift by setting the flyby velocity equal to the local dark-matter virial velocity,  $v_{\text{DM}} \approx 200 \text{ km s}^{-1}$ :

$$\delta f = \frac{v_{\text{DM}}}{c} f_p \approx 6.7 \times 10^{-4} \times f_p. \quad (4.15)$$

For the benchmark peak frequency  $f_p = 1.07$  GHz, this gives  $\delta f \approx 720$  kHz. Although this shift exceeds the instantaneous cavity bandwidth of ADMX ( $\Delta f_{\text{band}} \simeq f/Q \approx 13$  kHz) and would therefore displace the signal out of resonance during a naive fixed-frequency scan, it remains a small fraction of the full ADMX Run-1 frequency scan range ( $1.4 - 0.645$ ) GHz = 755 MHz. A flyby source would therefore be visible in some portion of the scan range, and a matched-filter search that accounts for a  $\pm 1$  MHz Doppler drift would recover the full signal duration.

We note, however, that the detectability problem identified in Sec. 4.3 is one of *strain* sensitivity, not frequency coverage: even at  $r = 1$  AU the strain falls roughly seven orders of magnitude below the ADMX threshold at 10 kpc, leaving a gap of  $\sim 3.5$  orders of magnitude after accounting for the  $1/r$  distance scaling from 10 kpc to 1 AU. The Doppler correction is therefore not the obstacle to detection.

## 5 Prospects for Observation at High-Frequency Gravitational-Wave Detectors

The detectability analysis of Sec. 4.3 shows that the characteristic strain of the binary-induced burst falls several orders of magnitude below the ADMX threshold at  $r = 10$  kpc, and that the threshold is reached only for  $r \lesssim 1$  AU. Whether such close encounters occur at any appreciable rate depends on the abundance and spatial distribution of PBHs, and on the statistics of PBH binary formation. Because the orbital separations that drive the  $\{2, 1, 1\} \rightarrow \{2, 1, -1\}$  resonant transition occur immediately prior to merger (Sec. 4.2), the question reduces to the local PBH merger rate filtered by the conditions on mass ratio and primary mass identified in Sec. 4.3:  $q \lesssim 10^{-2}$  and  $M_{\text{prim}} \lesssim 10^{-9} M_{\odot}$ .

In Ref. [37], merger rates were computed for PBHs formed in the early universe across four binary-formation channels and for generic mass functions. We focus on the *early two-body channel*, in which two neighboring PBHs form a gravitationally bound pair when their mutual attraction overcomes the Hubble flow. This channel is conceptually the cleanest, yields the most direct mapping to the  $(M_{\text{tot}}, q)$  space, and dominates the total merger rate at low  $f_{\text{PBH}}$ . The competing *early three-body channel*—dominant at large  $f_{\text{PBH}}$ —requires a treatment of N-body perturbations to the initial binary orbit and carries larger theoretical uncertainties [37]; we discuss its potential impact briefly in Sec. 5.3 below.

## 5.1 Merger Rate from the Early Two-Body Formation Channel

The double-differential merger rate density per unit logarithmic mass for the early two-body channel is [37]

$$\frac{dR_{E2}}{d \ln m_1 d \ln m_2} \approx \frac{1.6 \times 10^6}{\text{Gpc}^3 \text{ yr}} f_{\text{PBH}}^{53/37} \eta_{\text{PBH}}^{-34/37} \left( \frac{M_{\text{tot}}}{M_{\odot}} \right)^{-32/37} \left( \frac{t}{t_0} \right)^{-34/37} S_L S_E \psi(m_1) \psi(m_2), \quad (5.1)$$

where  $f_{\text{PBH}}$  is the PBH fraction of the dark-matter energy density,  $\eta_{\text{PBH}} \equiv \langle m \rangle^2 / \langle m^2 \rangle$  is the inverse normalized second moment of the mass function  $\psi(m)$  (not to be confused with the tidal mixing amplitude  $\eta$  of Eq. (4.7)),  $M_{\text{tot}} = m_1 + m_2$  is the total binary mass,  $t$  is the merger time, and  $t_0$  is the age of the universe. The suppression factor

$$S_L \approx \min \left\{ 1, 0.01 \left[ \left( \frac{t}{t_0} \right)^{0.44} f_{\text{PBH}} \right]^{-0.65} \exp \left( 0.03 \ln^2 \left[ \left( \frac{t}{t_0} \right)^{0.44} f_{\text{PBH}} \right] \right) \right\} \quad (5.2)$$

accounts for the disruption of PBH binaries by late-time large-scale structure, and

$$S_E \approx \frac{\sqrt{\pi} (5/6)^{21/74}}{\Gamma(29/37)} \left[ \frac{\langle m^2 \rangle / \langle m \rangle^2}{\bar{N}(y) + C} + \frac{\sigma_M^2}{f_{\text{PBH}}^2} \right]^{-21/74} e^{-\bar{N}(y)} \quad (5.3)$$

where

$$C = f_{\text{PBH}}^2 \frac{\langle m^2 \rangle / \langle m \rangle^2}{\sigma_M^2} \left\{ \left[ \frac{\Gamma(29/37)}{\sqrt{\pi}} U \left( \frac{21}{74}, \frac{1}{2}, \frac{5f_{\text{PBH}}^2}{6\sigma_M^2} \right) \right]^{-74/21} - 1 \right\}^{-1} \quad (5.4)$$

captures the suppression from Poisson fluctuations in the number of neighboring PBHs within the relevant comoving volume. Here  $\bar{N}(y)$  is the mean number of PBH neighbors within comoving separation  $y$ , and  $\sigma_M^2 / f_{\text{PBH}}^2$  is the variance of the mass-weighted density contrast [37].

The rate in Eq. (5.1) is evaluated at  $t = t_0$  (i.e., for mergers occurring today), which gives the present-day merger rate density  $R_{E2}(t_0)$  relevant for ADMX observations. We integrate over  $(m_1, m_2)$  via Monte-Carlo to obtain the portion of the rate associated with binaries in any chosen  $(M_{\text{prim}}, q)$  bin, using the relations  $q = m_1/m_2$  (with  $m_1 < m_2$  by convention) and  $M_{\text{prim}} = (1 + q) m_1$ .

## 5.2 Dichromatic Mass Function and Event Rates

To evaluate the merger rate for our benchmark system ( $M_{\text{prim}} = 6 \times 10^{-10} M_{\odot}$ ,  $q = 10^{-3}$ , so  $m_1 = 6 \times 10^{-10} M_{\odot}$ ,  $m_2 = 6 \times 10^{-13} M_{\odot}$ ), we examine two mass functions capable of producing large numbers of mixed-mass binary systems: a dichromatic mass function

$$\psi_{\text{di}}(m) = f_1 \delta(m - m_1) + f_2 \delta(m - m_2), \quad f_1 + f_2 = 1, \quad (5.5)$$

which places all PBH mass at two discrete values, and a double-lognormal mass function

$$\psi_{\text{dl}}(m) = \sum_{i=1}^2 \frac{f_i}{\sqrt{2\pi} \sigma m} \exp \left[ -\frac{\ln^2(m/m_i)}{2\sigma^2} \right], \quad f_1 + f_2 = 1. \quad (5.6)$$

Under Eq. (5.5) exactly three binary configurations are possible: equal-mass pairs at  $m_1$ , equal-mass pairs at  $m_2$ , and unequal-mass pairs  $(m_1, m_2)$  with  $q = 10^{-3}$ . Under Eq. (5.6),

Binary type	$q$	$R_{E2}$ [Gpc $^{-3}$ yr $^{-1}$ ]	ADMX-relevant?
$(m_1, m_1): 6 \times 10^{-10} + 6 \times 10^{-10} M_\odot$	1.0	$1.37 \times 10^{15}$	No
$(m_2, m_2): 6 \times 10^{-13} + 6 \times 10^{-13} M_\odot$	1.0	$2.79 \times 10^{14}$	No
$(m_1, m_2): 6 \times 10^{-10} + 6 \times 10^{-13} M_\odot$	$10^{-3}$	$2.79 \times 10^{14}$	<b>Yes</b>

**Table 3:** Present-day merger rate densities from the early two-body channel (Eq. (5.1)) for the dichromatic mass function (Eq. (5.5)) with  $m_1 = 6 \times 10^{-10} M_\odot$ ,  $m_2 = 6 \times 10^{-13} M_\odot$ , and  $f_{\text{PBH}} = 1$ . Only  $(m_1, m_2)$  binaries satisfy the ADMX detectability conditions  $q \lesssim 10^{-2}$  and  $M_{\text{prim}} \lesssim 10^{-9} M_\odot$  derived in Sec. 4.2.

there is greater allowed variation in  $M_{\text{prim}}$  and  $q$ , but most systems obtain parameters close to the previous three scenarios. As  $\sigma \rightarrow 0$ , the double lognormal case should reduce to the dichromatic case.

The resulting present-day merger rate densities, computed by Monte-Carlo integration of Eq. (5.1) with  $f_{\text{PBH}} = 1$  (all dark matter in PBHs, a conservative upper bound on the rate), are summarized in Table 3. The equal-mass  $(m_1, m_1)$  configuration dominates at  $R_{E2} = 1.37 \times 10^{15} \text{ Gpc}^{-3} \text{ yr}^{-1}$ . The unequal-mass  $(m_1, m_2)$  and equal-mass  $(m_2, m_2)$  configurations both yield  $R_{E2} \approx 2.79 \times 10^{14} \text{ Gpc}^{-3} \text{ yr}^{-1}$ . Only the  $(m_1, m_2)$  binaries satisfy the conditions  $q = 10^{-3}$  and  $M_{\text{prim}} = 6 \times 10^{-10} M_\odot$  required for a  $\{2, 1, 1\} \rightarrow \{2, 1, -1\}$  transition in the ADMX band (Sec. 4.3); this is the rate we use for the observation probability estimate.

### 5.3 Characteristic Detection Distance and the Strain Gap

Given a volumetric merger rate  $R_{E2}$  [Gpc $^{-3}$  yr $^{-1}$ ], the characteristic distance within which one event per year is expected is

$$d_{1\text{yr}} = \left( \frac{3}{4\pi R_{E2}} \right)^{1/3}, \quad (5.7)$$

obtained by setting the expected number of events in a sphere of radius  $d$  equal to unity:  $R_{E2} \cdot \frac{4}{3}\pi d^3 = 1$ . For the ADMX-relevant  $(m_1, m_2)$  rate  $R_{E2} = 2.79 \times 10^{14} \text{ Gpc}^{-3} \text{ yr}^{-1}$ , Eq. (5.7) gives

$$d_{1\text{yr}}^{(q=10^{-3})} \approx 9.1 \text{ kpc}. \quad (5.8)$$

At this distance, the characteristic strain from Sec. 4.3 falls  $\mathcal{O}(10^7)$  times below the ADMX sensitivity threshold  $h_{\text{min}} \sim 10^{-22}$ . The two detection requirements are therefore separately and jointly violated: the event rate is too low to place sources within  $\sim 1 \text{ AU}$ , and the strain is too small to detect events at the natural  $\sim 9 \text{ kpc}$  scale.

Figure 10 summarizes the characteristic distances  $d_{1\text{yr}}$  for all three binary classes in the dichromatic model. We find that a lognormal mass function centered on the same benchmark masses produces very similar results.

**Effect of PBH clustering.** Local overdensities of PBHs increase the effective merger rate by a factor  $\delta$  relative to the homogeneous prediction, which rescales all merger rates in Eq. (5.1) by  $\delta$  [37]. Since the event rate scales as  $R \propto \delta$ , the characteristic distance scales as  $d_{1\text{yr}} \propto \delta^{-1/3}$ . The most optimistic clustering estimates in the literature give  $\delta \lesssim 10^5$  [37],

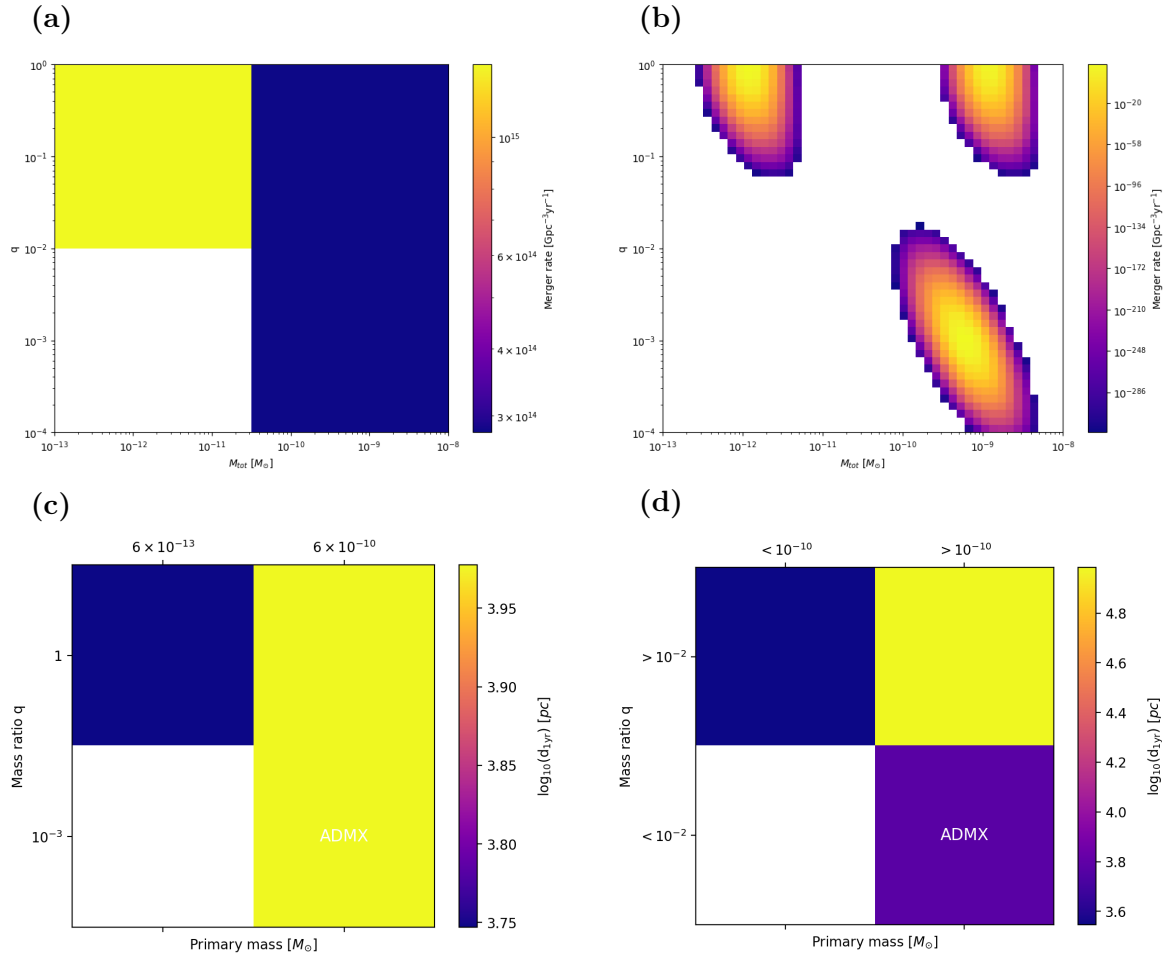


**Figure 10:** (a-b) Merger rates in  $M_{tot} - q$  space for dichromatic (a) and double lognormal (b) PBH mass functions with  $m_1 = 6 \times 10^{-10} M_\odot$ ,  $m_2 = 6 \times 10^{-13} M_\odot$ , and  $f_1 = f_2 = 0.5$  for both functions and  $\sigma = 0.05$  for the double lognormal. (c-d) Characteristic distances  $d_{1\text{yr}}$  (Eq. (5.7)) at which one merger per year is expected on average, for the dichromatic mass function (c) and for the double lognormal (d), subject to the binaries falling within a general range of benchmark parameters outlined in Sec. 4. For the dichromatic case, the three binary types correspond to those shown in Table 3. The ADMX-relevant  $(m_1, m_2)$  binaries (labeled “ADMX”) merge at appreciable rates only at  $d \gtrsim 9$  kpc for both mass functions, whereas ADMX requires  $r \lesssim 1$  AU to reach the detection threshold. The gap spans roughly eleven orders of magnitude in volume, or a factor of  $\sim 2 \times 10^7$  in strain.

which reduces  $d_{1\text{yr}}$  by a factor of  $(10^5)^{1/3} \approx 46$ :

$$d_{1\text{yr}}^{(\delta=10^5)} \approx \frac{9.1 \text{ kpc}}{46} \approx 200 \text{ pc}. \quad (5.9)$$

Even with this maximally optimistic clustering, the strain deficit at 200 pc remains  $\sim (200 \text{ pc}/1 \text{ AU}) \sim 4 \times 10^7$ —still seven orders of magnitude below the ADMX threshold. Extending to a rate of one event per decade ( $\delta = 10^5$ ) reduces  $d$  to  $\sim 100$  pc, with no qualitative improvement in the strain ratio.

## 5.4 Implications for Future Detectors

The analysis above identifies two independent, multiplicative obstacles to detecting binary-driven GA transitions at present-day cavity experiments:

1. *Strain deficit*: At the natural merger-rate distance  $d_{1\text{yr}} \approx 9\text{ kpc}$ , the signal strain is  $\sim 10^7$  times below the ADMX threshold. A factor-of- $10^7$  improvement in strain sensitivity, or equivalently a factor of  $10^{3.5} \approx 3000$  improvement in  $h_{\text{min}}$ , would be required from this factor alone.
2. *Rate deficit*: Reducing the detection distance to  $\lesssim 1\text{ AU}$  requires a rate enhancement of  $(9\text{ kpc}/1\text{ AU})^3 \sim 10^{33}$  over the homogeneous prediction—far beyond what any clustering model can provide.

These obstacles together imply that a qualitative change in experimental approach, rather than incremental improvements to existing cavities, is necessary for binary-GA signals to become observable. The specific detector properties that would help most are: (i) a factor of  $\sim 10^{3.5}$  improvement in strain sensitivity  $h_{\text{min}}$ , achievable in principle through larger cavity volume, stronger magnetic field, or lower system temperature; (ii) faster ring-up times  $\tau_{\text{ring}}$ , which extend the detectable mass-ratio range to larger  $q$  and thereby increase the event rate; and (iii) broader frequency coverage at lower frequencies, since the GW frequency scales as  $f_p \propto M_{\text{BH}}^{-1}$  (Sec. 2) and heavier PBHs—which are more abundant—produce sub-GHz signals outside the current ADMX scan range.

The isolated-GA annihilation and level-transition signals studied in Sec. 3 are not subject to the same rate limitations, since they arise from persistent, continuous emission rather than merger events. Their detectability is governed instead by the peak strain at a given distance, with  $h_{0,\text{ann}}^{\text{peak}} \sim 10^{-22}$  at 1 kpc (Eq. (3.18)). For sources within  $\sim 1\text{ kpc}$ —well within the Milky Way PBH halo—the annihilation signal of an isolated GA is a more promising target for current ADMX-band experiments than the binary-induced burst, and we highlight it as the primary observational target for near-term searches.

## 6 Discussion and Conclusions

We have presented a unified treatment of high-frequency gravitational-wave emission from superradiant boson clouds around primordial black holes, covering both isolated gravitational atoms and binary-perturbed systems. In this section we synthesize the main results, place them in the context of the broader superradiance and high-frequency GW literature, discuss the principal caveats and uncertainties, and identify the most promising directions for future work.

### 6.1 Summary and Key Conclusions

**Parameter space and Regge trajectories (Sec. 2).** The gravitational fine-structure constant  $\alpha = GM_{\text{BH}}\mu$  determines both the efficiency of superradiant cloud growth and the frequency of the emitted GWs. For efficient superradiance ( $\alpha \in [0.05, 0.5]$ ) and GW emission in the MHz–GHz band, the superradiance condition selects boson masses  $\mu \sim 10^{-8}\text{--}10^{-5}\text{ eV}$  and, through  $M_{\text{BH}} = \alpha/(G\mu)$ , host BH masses  $M_{\text{BH}} \sim 10^{-6}\text{--}10^{-3}\text{ }M_{\odot}$ —precisely the primordial BH mass window (Table 1). The Regge trajectories make this mapping explicit: each allowed  $(M_{\text{BH}}, \mu, m)$  configuration traces a curve in the  $(a_*, M_{\text{BH}})$  plane along which the cloud grows, extracts angular momentum, and emits narrowband GWs. The maximum cloud mass

fraction of 10.81%, obtained numerically for  $\alpha \approx 0.2$  and  $a_* \rightarrow 1$ , is in excellent agreement with the analytic upper bound of Ref. [32].

**Isolated gravitational atom (Sec. 3).** For an isolated GA we computed time-domain waveforms for both the level-transition and boson-annihilation channels, together with analytic frequency-domain templates (Appendix A). The key quantitative results are:

- *Annihilation:* peak strain  $h_{0,\text{ann}}^{\text{peak}} \simeq 10^{-22}$  at  $r = 1$  kpc, with emission frequency  $f_{\text{ann}} \simeq \mu/\pi \approx 96$  MHz for the benchmark system ( $\mu_a = 2 \times 10^{-7}$  eV,  $M_{\text{BH}} = 3.1 \times 10^{-4} M_{\odot}$ ,  $\alpha = 0.43$ ). The signal is effectively a monochromatic steady source with a decay timescale  $\tau_{\text{ann}} \sim 10^{25}\text{--}10^{60}$  yr, enormously exceeding both the Hubble time and any observation window.
- *Level transitions:* peak strain  $h_{0,\text{tr}}^{\text{peak}} \simeq 10^{-23}$  at  $r = 1$  kpc, with emission frequency  $f_{\text{tr}} \simeq 526$  MHz for the  $\{6, 4, 4\} \rightarrow \{5, 4, 4\}$  benchmark. The signal lifetime  $\tau_{\text{tr}} \sim 10^3\text{--}10^6$  yr is long compared to any observation period but finite, giving a spectral width  $\Delta f \sim \tau_{\text{tr}}^{-1}/(2\pi) \ll 1$  Hz.
- The frequency-domain templates take analytic closed forms: an exponential-integral  $E_1$  expression for the annihilation signal, and a complex Lorentzian shifted by the carrier frequency  $\omega_{\text{ann}}$  or  $\omega_{\text{tr}}$  for the two polarizations (Appendix A). Both signals trivially satisfy the cavity ring-up condition  $\tau_{\text{signal}} \gg \tau_{\text{ring}} \sim 10^{-5}$  s.

**Binary-perturbed gravitational atom (Secs. 4 and 5).** Applying the Landau–Zener resonance formalism of Ref. [29] to PBH binaries, we computed the characteristic strain of the transient GW burst produced when the binary sweeps through the  $\{2, 1, 1\} \rightarrow \{2, 1, -1\}$  hyperfine transition. The principal results are:

- The peak GW frequency  $f_p$  (Eq. (4.9)) lies naturally in the GHz band for host BH masses  $M_{\text{BH}} \sim 10^{-9}\text{--}10^{-10} M_{\odot}$  at  $\alpha \approx 0.2$ , confirming that PBH binaries are the only astrophysical system that can populate the ADMX frequency range through binary-induced superradiance.
- The ring-up condition  $\Delta t \gtrsim \tau_{\text{ring}}$  is satisfied throughout the allowed  $(\alpha, q)$  parameter space at the benchmark mass ratio  $q = 10^{-3}$ , regardless of resonant frequency. This is a necessary but not sufficient condition for detection.
- The GW characteristic strain at  $r = 10$  kpc falls *several orders of magnitude* below the ADMX threshold  $h_{\text{min}} \sim 10^{-22}$ . Detection would require sources within  $r \lesssim 1$  AU.
- The early two-body PBH merger rate [37] evaluated for the benchmark dichromatic mass function gives a characteristic event distance  $d_{1\text{yr}} \approx 9.1$  kpc for ADMX-relevant ( $q = 10^{-3}$ ) binaries. Even with the maximally optimistic PBH clustering factor  $\delta \sim 10^5$ , this reduces only to  $\approx 200$  pc—still seven orders of magnitude in strain below the ADMX threshold. We conclude that binary-driven level-transition events are not detectable with current ADMX sensitivity.

## 6.2 Comparison to Related Work

The GW signatures of superradiant clouds around *stellar-mass* BHs are well studied [15–18], with constraints on ultralight bosons from LIGO/Virgo spin measurements and non-detections

of continuous GWs establishing the most robust exclusion regions in the  $(\mu, M_{\text{BH}})$  plane for  $\mu \sim 10^{-13}$ – $10^{-11}$  eV [19, 21]. The present work extends this program into qualitatively new territory in two respects.

First, by focusing on PBH masses  $M_{\text{BH}} \lesssim 10^{-3} M_{\odot}$  we access boson masses  $\mu \sim 10^{-7}$ – $10^{-5}$  eV for which no spin-measurement constraints currently exist, and GW frequencies in the MHz–GHz range that are inaccessible to LIGO-band searches. High-frequency GW experiments such as ADMX and the broadband detectors proposed in Refs. [2, 3] offer the only existing instrumental sensitivity in this band; our frequency-domain templates (Appendix A) provide the waveform targets needed for a matched-filter search.

Second, the binary-perturbation analysis builds directly on the Baumann–Chia–Porto (BCP) Landau–Zener framework [27, 28] and the recent extension by Kyriazis & Yang [29], which derived the analytic GW strain template for tidally driven transitions. Previous applications of the BCP formalism focused primarily on the depletion of clouds (floating orbits, inspiral modifications, dephasing of the binary GW signal) in the context of LISA-band sources [27, 28, 30, 31], and on the resonance history in Ref. [32]. We are the first to apply the Kyriazis & Yang waveform template to PBH binaries in the MHz–GHz regime and to compare it directly to the sensitivity of an existing high-frequency detector, yielding a quantitative (negative) detectability result rather than a parametric estimate.

The bosonova bound on the cloud occupation number, following Refs. [25, 26], is found to be non-restrictive for QCD-axion-like couplings ( $f_a \sim 10^{16}$  GeV) in the bulk of our PBH parameter space (Eq. (2.13)), so the strain amplitudes we derive are not suppressed by bosonova cycling. For very weakly coupled bosons ( $f_a \ll M_{\text{Pl}}$ ) the cloud would cycle and the strain would be reduced; we note this as a limitation and leave the quantitative treatment of bosonova-modified waveforms to future work.

### 6.3 Caveats and Limitations

Several idealizations warrant discussion.

**Spin distribution of PBHs.** Our strain calculations assume near-extremal initial spin  $a_* \rightarrow 1$ , which maximizes the extractable angular momentum and thus  $N_{\text{sat}}$ . The actual spin distribution of PBHs formed in the early universe depends on their formation mechanism: radiation-era collapse generically produces near-zero spins [39], while mergers and accretion can spin up BHs over time. If PBHs form with low spins, the superradiant cloud may never reach  $N_{\text{sat}}$ , reducing both the peak strain and the signal duration. Our results should therefore be interpreted as upper bounds on the GW signal amplitude for a given  $(\mu, M_{\text{BH}}, \alpha)$  combination.

**Isolated versus binary GAs.** We have treated the isolated and binary channels independently, but in a realistic PBH population both may be active simultaneously or sequentially. Binary companions that sweep through resonance before the isolated cloud reaches saturation will partially deplete the cloud, suppressing the subsequent annihilation and level-transition signals [32]. Conversely, an isolated cloud that has already undergone significant annihilation before the binary resonance is crossed will produce a weaker binary-induced burst than our estimates suggest. A self-consistent treatment that evolves both channels simultaneously remains to be carried out.

**Multi-level dynamics.** Our binary waveform analysis follows Ref. [29] in treating the  $\{2, 1, 1\} \rightarrow \{2, 1, -1\}$  transition as a two-level system. In reality, multiple superradiant

levels may be populated simultaneously (Fig. 4), and the binary may sweep through several resonances in succession before merger. The resonance history can be complex and depends on the level hierarchy and the chirp timescale [32]; multi-level corrections to the waveform template are beyond the scope of this paper.

#### 6.4 Outlook and Future Directions

Despite the negative detectability conclusion for binary-induced bursts at current ADMX sensitivity, several physically well-motivated avenues remain open.

**Isolated-GA annihilation as a near-term target.** The isolated-GA annihilation signal ( $h_{0,\text{ann}}^{\text{peak}} \sim 10^{-22}$  at 1 kpc,  $f_{\text{ann}} \sim \text{MHz-GHz}$ ) is not subject to the event-rate limitations that render binary-driven bursts undetectable. For PBHs distributed throughout the Milky Way dark-matter halo, sources within  $\sim 1$  kpc are plausibly present with an abundance proportional to the local PBH dark-matter fraction  $f_{\text{PBH}}$ . The continuous, monochromatic nature of the signal ( $\tau_{\text{ann}} \gg t_{\text{Hubble}}$ ,  $\Delta f \lesssim 10^{-33}$  Hz) makes it an ideal target for coherent integration strategies that accumulate signal-to-noise over extended observation periods. We identify this channel as the primary observational target within the current ADMX band, and provide the explicit  $E_1$ -based frequency-domain template (Appendix A.1) needed to implement a matched-filter search.

**Next-generation detector requirements for binary signals.** For binary-induced bursts to become detectable, three improvements are needed in combination: (i) a factor of  $\sim 10^{3.5}$  improvement in strain sensitivity  $h_{\text{min}}$  (Eq. (4.14)), achievable through larger cavity volume, stronger magnetic field, and reduced system temperature; (ii) broader frequency coverage, particularly at sub-GHz frequencies where heavier and potentially more abundant PBHs contribute; and (iii) faster ring-up times  $\tau_{\text{ring}}$ , which relax the constraint on the signal duration  $\Delta t$  and thereby open parameter space at larger mass ratios  $q$ . Novel detector concepts—plasma haloscopes, LC circuit detectors, and broadband bulk acoustic resonators [2, 3]—may provide complementary sensitivity in frequency ranges not covered by ADMX.

**Constraints on the ultralight boson spectrum.** Even without a detection, the non-observation of a persistent narrowband GW signal at a given frequency places an upper bound on the product  $f_{\text{PBH}} \cdot h_{0,\text{ann}}^{\text{peak}}$ , which translates into a constraint on the PBH density in the local dark-matter halo as a function of boson mass. Deriving quantitative spin-down constraints analogous to those obtained from LIGO-band continuous-wave searches [19, 21], but using ADMX non-detection data, is a direct application of the templates presented in this paper and represents a novel intersection of axion dark-matter searches with GW physics.

**PBH spin distribution and formation constraints.** The sensitivity of the GW strain to the initial BH spin (through  $N_{\text{sat}} \propto a_* - a_*^{\text{crit}}$ ) makes PBH-GA systems a probe of PBH formation mechanisms, complementary to mass-function constraints from microlensing and CMB observations [22]. A statistical population analysis combining the GW signal distribution with the PBH spin distribution would allow simultaneous constraints on both the PBH abundance and their formation spin, and is facilitated by the analytic templates derived here.

In sum, in this paper we have systematically studied the MHz–GHz gravitational-wave signatures of superradiant boson clouds around primordial black holes. Our results establish PBH–gravitational atom systems as among the very few theoretically well-motivated sources of high-frequency gravitational waves, and provide the complete set of waveform templates needed for targeted searches at ADMX and successor experiments. The gap between current sensitivity and the predicted signal levels defines a concrete engineering target for next-generation high-frequency GW detectors, and the boson mass range  $\mu \sim 10^{-7}$ – $10^{-5}$  eV probed by these signals remains largely unconstrained by any other observational technique.

Primordial black hole–gravitational atom systems provide one of the few theoretically well-motivated sources of MHz–GHz gravitational waves. While isolated systems can produce long-lived, narrow-band signals with potentially observable strain amplitudes under optimistic conditions, binary-induced transients are generically suppressed both in amplitude and event rate. This study highlights a clear experimental target: improved strain sensitivity, broader frequency coverage, and faster detector response times are all essential to probe this class of signals. Finally, the analytic templates developed here provide concrete benchmarks for future high-frequency gravitational-wave searches.

## Acknowledgements

We are grateful to Giovanni Maria Tomaselli and Antonios Kyriazis for useful clarifications and discussions. LB, CE, and SP are supported in part by the U.S. Department of Energy, Office of Science, Office of High Energy Physics of U.S. Department of Energy under grant Contract Number DE-SC010107 (to SP).

## A Frequency Domain Strain Templates

The detectability of a gravitational-wave signal is most cleanly expressed in terms of the characteristic strain, which is defined from the Fourier transform of the metric perturbation as  $h_c(f) = 2f|\tilde{h}(f)|$ . While the raw Fourier amplitude  $\tilde{h}(f)$  depends on the details of the observation, such as the total duration of the time series and the specific sampling, the combination  $h_c(f)$  isolates the physically relevant quantity: the accumulated signal power at a given frequency, including the contribution from the number of coherent wave cycles. For a quasi-monochromatic source observed over an observation time  $T$ , one has approximately  $h_c(f_0) \sim h_0\sqrt{f_0T}$ , so that the characteristic strain increases with the square root of the effective number of cycles. This makes  $h_c(f)$  the appropriate quantity for comparing theoretical signals to the sensitivity of gravitational-wave detectors.

A detector is characterized by its one-sided noise power spectral density  $S_n(f)$ . The corresponding noise amplitude is given by  $h_n(f) = \sqrt{fS_n(f)}$ . Signal power and detector noise are compared at the same level: both  $h_c(f)$  and  $h_n(f)$  have the same dimensions and represent amplitudes per logarithmic frequency interval. A source is detectable when its characteristic strain exceeds the noise curve, and the expected signal-to-noise ratio is

$$SNR^2 = \int_0^\infty \frac{h_c^2(f)}{f^2 S_n(f)} df = \int_0^\infty \frac{h_c^2(f)}{h_n^2(f)} d(\ln f). \quad (\text{A.1})$$

This expression shows explicitly why  $h_c(f)$  is the correct quantity to compare with detector sensitivity. Any direct comparison using  $\tilde{h}(f)$  alone would be misleading, because  $\tilde{h}(f)$  scales with the chosen Fourier window and does not represent a physical amplitude.

In the context of black hole superradiance and axion annihilation or level transitions, the characteristic strain provides a unified language for evaluating detectability against detector strain curves. The signals are intrinsically narrow-band and can be long-lived, so  $h_c(f)$  reflects both the instantaneous gravitational-wave amplitude and the coherence of the emission process. Even if the raw strain is extremely small, the large number of coherent cycles at the transition or annihilation frequency can raise  $h_c(f)$  above detector noise. Once expressed in terms of  $h_c(f)$ , the comparison to detector sensitivity curves is immediate: gravitational-wave observatories are sensitive to signals whenever  $h_c(f)$  lies above (or not far below)  $h_n(f)$  at the relevant frequency. This is the fundamental criterion for detection prospects.

### A.1 Annihilation Strain

The bulk of this paper has shown that there are multiple potentially detectable signals in a gravitational atom system. These signals can arise from both an isolated gravitational atom or due to the presence of a binary companion. In the first case, we have shown that detectable signals arise from two separate phenomenon: level transitions and boson annihilations.

The first frequency domain strain that we consider arises due to the axion annihilation within a specified level. Again, the time domain strain is specified in Eq (3.15) and the only time dependence arises from the decay of the state population in Eq. (3.14):

$$h_{0,\text{ann}}(t) = \frac{N_{\text{max}}}{1 + \Gamma_a N_{\text{max}} t} \sqrt{\frac{4G_N}{r^2 \omega_{\text{ann}}} \Gamma_a} \quad (\text{A.2})$$

where again we have made the assumptions that  $\alpha$  and the superradiance rates are unchanging in time to obtain an approximate form of the annihilation strain amplitude. Again, this allows us to take a fourier transform to obtain an analytic form of the annihilation strain as a function of frequency. We begin with the one-sided Fourier transform,

$$\tilde{h}_{0,\text{ann}}(\omega) = \frac{1}{\sqrt{2\pi}} \int_0^\infty \frac{A e^{-i\omega t}}{1 + \beta t} dt, \quad \beta > 0, \quad (\text{A.3})$$

where we will consistently use the convention of  $f = \frac{\omega}{2\pi}$ .

$$A = N_{\text{max}} \sqrt{\frac{4G_N \Gamma_a}{r^2 \omega_{\text{ann}}}}, \quad \beta = \Gamma_a N_{\text{max}}. \quad (\text{A.4})$$

Let  $u = 1 + \beta t$ , so that  $t = (u - 1)/\beta$  and  $dt = du/\beta$ . Substituting, we find

$$\tilde{h}_{0,\text{ann}} = \frac{A}{\sqrt{2\pi} \beta} e^{i\omega/\beta} \int_1^\infty \frac{e^{-i(\omega/\beta)u}}{u} du. \quad (\text{A.5})$$

To evaluate the integral, we introduce a causal regulator  $+i\epsilon$  to ensure convergence and define the exponential integral  $E_1(x)$  in its equivalent forms:

$$E_1(x) \equiv \int_1^\infty \frac{e^{-tx}}{t} dt = \int_x^\infty \frac{e^{-u}}{u} du, \quad (|\arg x| < \pi). \quad (\text{A.6})$$

Comparing with Eq. (A.5), we immediately identify

$$x = i \frac{\omega}{\beta} + i\epsilon,$$

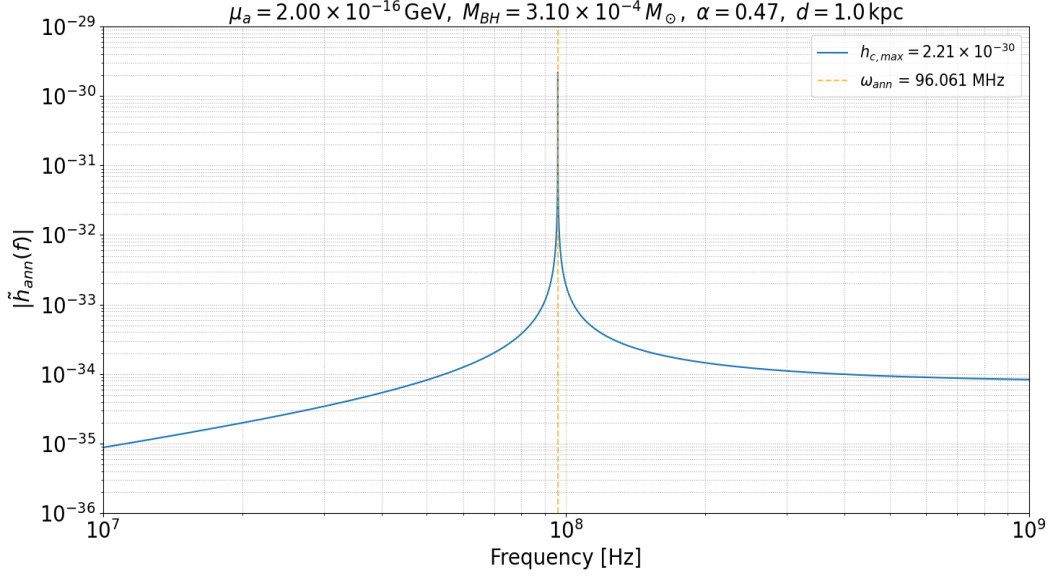


**Figure 11:** Characteristic strain of the Fourier transform for the annihilation strain. Input parameters match those from Fig. 5.

where the infinitesimal imaginary term  $+i\epsilon$  enforces the causal ( $+i\epsilon$ ) prescription. Thus,

$$\int_1^\infty \frac{e^{-i(\omega/\beta)u}}{u} du = E_1\left(i\frac{\omega}{\beta} + i\epsilon\right). \quad (\text{A.7})$$

Substituting Eq. (A.7) into Eq. (A.5), we obtain the compact result

$$\tilde{h}_{0,\text{ann}} = \frac{A}{\sqrt{2\pi}\beta} e^{i\omega/\beta} E_1\left(i\frac{\omega}{\beta} + i\epsilon\right), \quad (\text{A.8})$$

where  $i\epsilon$  denotes the same causal regulator used in the definition of  $E_1$ . To rewrite Eq. (A.8) in terms of the exponential integral  $\text{Ei}$  and more familiar functions, we use the relation

$$E_1(z) = -\text{Ei}(-z), \quad (\text{A.9})$$

and continue it to complex arguments along the causal branch. For imaginary arguments, the continuation gives

$$\text{Ei}(ix + i\epsilon) = \text{PV}[\text{Ei}(ix)] + i\pi\text{Sign}(x), \quad (\text{A.10})$$

where  $\text{PV}[\text{Ei}(ix)]$  refers to the principal value of the exponential integral and the second term represents the usual  $i\pi$  phase picked up when crossing the branch. Similarly, the logarithm acquires the standard phase shift across its branch cut,

$$\log(i\omega) - \log(-i\omega) = i\pi\text{Sign}(\omega), \quad (\text{A.11})$$

corresponding to the same causal choice of branch.

Using Equations (A.9)-(A.11), we can rewrite equation (A.8) as:

$$\tilde{h}_{0,\text{ann}} = \frac{A}{\sqrt{2\pi}\beta} e^{i\omega/\beta} \left[ -2\text{Ei}\left(\frac{i\omega}{\beta}\right) + (\log(i\omega) - \log(-i\omega)) \right]. \quad (\text{A.12})$$

Finally, restoring  $A$  and  $\beta = \Gamma_a N_{\max}$  gives

$$\tilde{h}_{0,\text{ann}}(\omega) = \frac{N_{\max}}{\sqrt{2\pi}} \sqrt{\frac{4G_N}{r^2\omega_{\text{ann}}}} e^{-i\omega/(\Gamma_a N_{\max})} \left[ -2 \text{Ei}\left(\frac{i\omega}{\Gamma_a N_{\max}}\right) + i\pi \text{Sign}(\omega) \right], \quad (\text{A.13})$$

which is identical to (A.12) upon using (A.11) and restoring all constants.

In order to return the oscillatory term to our frequency domain template, we need to multiply the envelope by  $e^{\pm i\omega_{\text{ann}}t}$ . This has the effect of shifting our frequency, so we can describe the Fourier transform of our envelope as:

$$\mathcal{F}[h_0(t) e^{\pm i\omega_{\text{ann}}t}] = \tilde{h}(\omega \mp \omega_{\text{ann}}) \quad (\text{A.14})$$

With  $\cos = \frac{1}{2}(e^{i\phi_0} e^{i\omega_{\text{ann}}t} + e^{-i\phi_0} e^{-i\omega_{\text{ann}}t})$ ,  $\sin = \frac{1}{2i}(e^{i\phi_0} e^{i\omega_{\text{ann}}t} - e^{-i\phi_0} e^{-i\omega_{\text{ann}}t})$ , the polarization spectra are

$$\tilde{h}_+(\omega) = \frac{1 + \cos^2(\iota)}{4} \left[ e^{i\phi_0} \tilde{h}(\omega - \omega_{\text{ann}}) + e^{-i\phi_0} \tilde{h}(\omega + \omega_{\text{ann}}) \right], \quad (\text{A.15})$$

$$\tilde{h}_\times(\omega) = \frac{\cos(\iota)}{2i} \left[ e^{i\phi_0} \tilde{h}(\omega - \omega_{\text{ann}}) - e^{-i\phi_0} \tilde{h}(\omega + \omega_{\text{ann}}) \right]. \quad (\text{A.16})$$

Substituting  $\tilde{h}$  gives the explicit closed forms:

$$\tilde{h}_+(\omega) = \frac{N_{\max}}{\sqrt{2\pi}} \sqrt{\frac{4G_N}{r^2\omega_{\text{ann}}}} \frac{1 + \cos^2(\iota)}{4} \left[ e^{i\phi_0} e^{i(\omega - \omega_{\text{ann}})/\beta} \left( -2 \text{Ei}\left(\frac{i(\omega - \omega_{\text{ann}})}{\beta}\right) + i\pi \text{Sign}(\omega - \omega_{\text{ann}}) \right) \right. \\ \left. + e^{-i\phi_0} e^{i(\omega + \omega_{\text{ann}})/\beta} \left( -2 \text{Ei}\left(\frac{i(\omega + \omega_{\text{ann}})}{\beta}\right) + i\pi \text{Sign}(\omega + \omega_{\text{ann}}) \right) \right], \quad (\text{A.17})$$

$$\tilde{h}_\times(\omega) = \frac{N_{\max}}{\sqrt{2\pi}} \sqrt{\frac{4G_N}{r^2\omega_{\text{ann}}}} \frac{\cos(\iota)}{2i} \left[ e^{i\phi_0} e^{i(\omega - \omega_{\text{ann}})/\beta} \left( -2 \text{Ei}\left(\frac{i(\omega - \omega_{\text{ann}})}{\beta}\right) + i\pi \text{Sign}(\omega - \omega_{\text{ann}}) \right) \right. \\ \left. - e^{-i\phi_0} e^{i(\omega + \omega_{\text{ann}})/\beta} \left( -2 \text{Ei}\left(\frac{i(\omega + \omega_{\text{ann}})}{\beta}\right) + i\pi \text{Sign}(\omega + \omega_{\text{ann}}) \right) \right]. \quad (\text{A.18})$$

## A.2 Isolated Level Transition Strain

We next develop a frequency domain template of the transition amplitude gravitational strain outlined in Eq. (3.7) by taking a Fourier transform of the approximate solution. Since both the states grow exponentially and approximately independently for the majority of the lifetime of the excited state, we will be approximating the form of both the ground and excited states as  $\frac{dN_g}{dt} = \Gamma_g^{sr} N_g + \Gamma_t N_g N_e$  and  $\frac{dN_e}{dt} = \Gamma_e^{sr} N_e - \Gamma_t N_g N_e$ . The resulting time dependence of each state is then an exponential of the form  $N_g(t) = N_0 \exp\{(\Gamma_g^{SR} + \Gamma_t N_e)t\}$  and  $N_e(t) = N_0 \exp\{(\Gamma_e^{SR} + \Gamma_t N_g)t\}$ . The transition amplitude as a function of time, assuming a constant in time superradiant transition rate  $\Gamma_t$ , gives us a transition strain of the form

$$h_{0,tr} \approx \sqrt{\frac{4G_N}{r^2\omega_{tr}}} \Gamma_t N_0^g N_0^e \exp\{(\Gamma_e^{sr} + \Gamma_g^{sr} + \Gamma_t N_g - \Gamma_t N_e)t\} \quad (\text{A.19})$$

Under these approximations we can take a Fourier transform to find the functional form of our strain. Doing so, we obtain the following expression:

$$h_{0,tr}(\omega) = \frac{1}{2\pi} \frac{\sqrt{\frac{4G_N}{r^2\omega_{tr}}} \Gamma_t N_0^g N_0^e}{(\Gamma_e^{sr} + \Gamma_g^{sr} + \Gamma_t N_g - \Gamma_t N_e - i\omega)} \left( -1 + \exp[(\Gamma_e^{sr} + \Gamma_g^{sr} + \Gamma_t N_g - \Gamma_t N_e - i\omega)T] \right) \quad (\text{A.20})$$

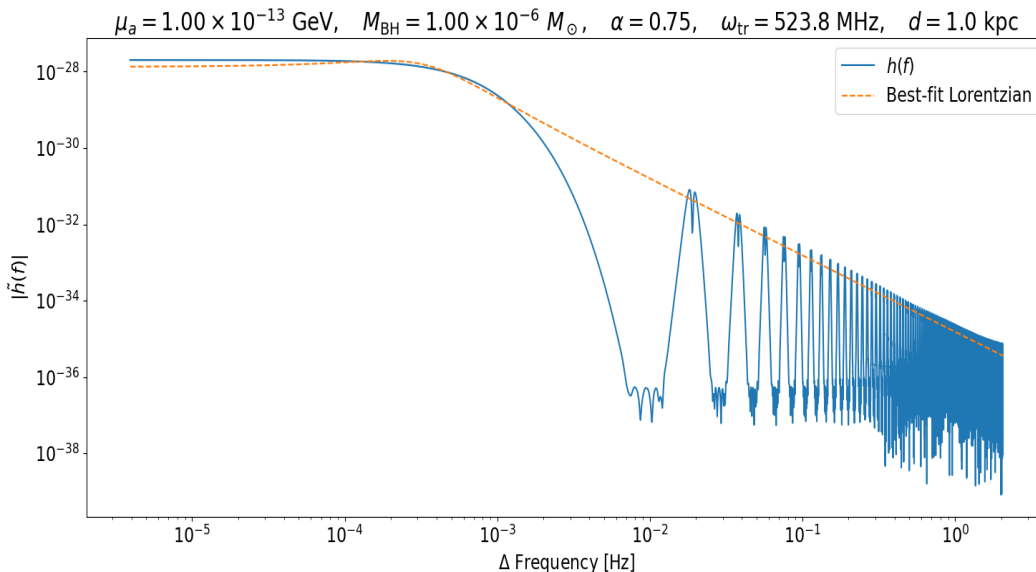


**Figure 12:** Characteristic strain of the Fourier transform for the level transition strain. X-axis is plotted as a function of frequency offset  $\Delta f = f - f_{tr}$ . Input parameters match those from Fig. 3. The direct FFT is outlined in blue, which includes oscillations originating from numerical artifacts. Also shown is the expected Lorentzian shape of the signal with parameters matching the frequency domain level transition strain. The width of the signal is set by the transition rate  $\Gamma_{tr}$ , whereas the carrier frequency  $\omega_{tr}$  is set by the boson mass.

with  $T$  being the time taken from the start of superradiance to when the excited state has transitioned completely. This is the approximate form of our gravitational wave signal in the frequency domain due to level transitions within the gravitational atom. Since detectors look at the frequency decomposition of these signals, this is ultimately the desired form for the gravitational strain. Again, to include the physical oscillations of the gravitational wave and its orientation, we can treat the transition signal as an amplitude (or envelope) modulated by a carrier frequency corresponding to the transition energy. In other words, the total strain is just our smooth envelope multiplied by an oscillatory factor at  $\omega_{tr}$ :

$$h_{tr}(t) = h_{0,tr}(t) \cos(\omega_{tr}t + \phi_0) = \frac{1}{2} h_{0,tr}(t) \left( e^{i(\omega_{tr}t + \phi_0)} + e^{-i(\omega_{tr}t + \phi_0)} \right).$$

When we Fourier transform this, the oscillatory pieces simply shift the spectrum to  $\pm\omega_{tr}$ , giving

$$\mathcal{F}[h_{tr}^{\text{env}}(t)e^{\pm i\omega_{tr}t}] = \tilde{h}_{tr}^{\text{env}}(\omega \mp \omega_{tr}). \quad (\text{A.21})$$

So the frequency-domain strain becomes two terms centered on the transition frequency, each weighted by the phase  $\phi_0$ :

$$\tilde{h}_{tr}(\omega) = \frac{1}{2} \left[ e^{i\phi_0} \tilde{h}_{0,tr}(\omega - \omega_{tr}) + e^{-i\phi_0} \tilde{h}_{0,tr}(\omega + \omega_{tr}) \right]. \quad (\text{A.22})$$

Finally, we can include the detector-frame polarization dependence. The observed strain depends on the inclination angle  $\iota$  of the system relative to the line of sight. The two standard

polarizations then take the form

$$\tilde{h}_{\text{tr}}^{(+)}(\omega) = \frac{1 + \cos^2 \iota}{4} \left[ e^{i\phi_0} \tilde{h}_{\text{tr}}^{\text{env}}(\omega - \omega_{\text{tr}}) + e^{-i\phi_0} \tilde{h}_{\text{tr}}^{\text{env}}(\omega + \omega_{\text{tr}}) \right], \quad (\text{A.23})$$

$$\tilde{h}_{\text{tr}}^{(\times)}(\omega) = \frac{\cos \iota}{2i} \left[ e^{i\phi_0} \tilde{h}_{\text{tr}}^{\text{env}}(\omega - \omega_{\text{tr}}) - e^{-i\phi_0} \tilde{h}_{\text{tr}}^{\text{env}}(\omega + \omega_{\text{tr}}) \right]. \quad (\text{A.24})$$

These two polarizations represent the characteristic “plus” and “cross” patterns of the transition signal, differing only by a relative phase and the inclination weighting. In practice, both appear as narrow peaks in the frequency spectrum at  $\omega_{\text{tr}}$ , modulated by the growth and decay encoded in  $\tilde{h}_{\text{tr}}^{\text{env}}(\omega)$ . The plot above shows the characteristic strain for a set of parameters which would produce gravitational waves in the MHz range (Fig. 12). The spectral width  $\Delta\omega$  of the template is controlled entirely by the characteristic timescale over which the envelope  $A(t)$  varies (i.e. by the relevant superradiant and transition rates),

$$\Delta\omega \sim \Gamma_{\text{tot}} \sim \mathcal{O}(\text{yr}^{-1}) \Rightarrow \Delta f \sim \frac{\Delta\omega}{2\pi} \ll 1 \text{ Hz}, \quad (\text{A.25})$$

even though the line is centered at  $f_{\text{tr}} = \omega_{\text{tr}}/2\pi \sim \text{MHz}$ . Consequently, the frequency-domain signal appears as an extremely narrow (sub-Hz) Lorentzian line located at the MHz transition frequency. In general, the carrier frequency fixes the centering of the line position, while the slow population evolution ( $\mathcal{O}(10^3)$  years) sets the linewidth. Faster population evolutions will therefore result in Lorentzian signals with much wider frequency resolution, whereas slowly evolving states will appear as increasingly narrow, near-monochromatic lines in the frequency spectrum.

### A.3 Binary Level Transition Strain

The frequency domain template for the “plus” polarization for binary level transition strain given within Eq. (4.1) is already defined by Eq. (4.5), where a detailed derivation using the stationary phase approximation can be found within [29]. The frequency domain template for the “cross” polarization can also be easily obtained using the same method: Rewriting Eq. (4.2) into the form of:

$$h_{\times,211}(t) = h_0 \cos \iota \left[ \frac{e^{-2i\Delta m\varphi(t)} Q(t) - e^{2i\Delta m\varphi(t)} Q^*(t)}{2i} \right] \quad (\text{A.26})$$

by expanding the imaginary component, then plugging into the integral of:

$$\tilde{h}_{+, \times}(\omega) = \int dt h_{+, \times}(t) e^{i\omega t}. \quad (\text{A.27})$$

we obtain the following expression:

$$\tilde{h}_{\times}(\omega) = \frac{h_0 \cos \iota}{2i} \int dt \left[ e^{i\omega t - 2i\Delta m\varphi(t)} Q(t) - e^{i\omega t + 2i\Delta m\varphi(t)} Q^*(t) \right] \quad (\text{A.28})$$

Evaluating the integral through the same method of stationary phase approximation within [29] with the same arguments so that the first integral vanishes, we obtain:

$$\tilde{h}_{\times}(\omega) = -\frac{\sqrt{\pi} h_0 \cos \iota}{2i \sqrt{\gamma |\Delta m|}} Q^*(t_+(\omega)) e^{i\Psi_+(\omega)} \quad (\text{A.29})$$

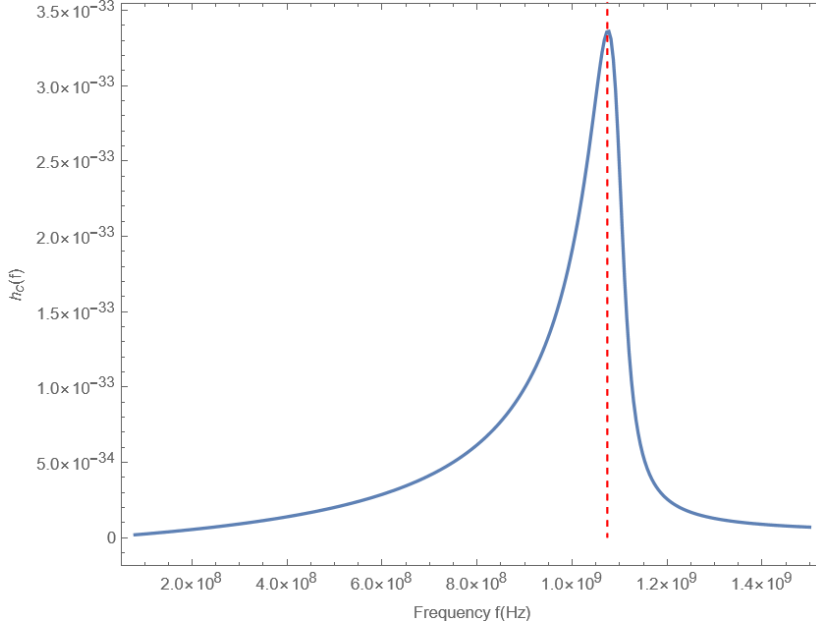


**Figure 13:** Computation of the binary perturbation characteristic strain  $h_c(f) = 2f|\tilde{h}(f)|$  with  $\tilde{h}(f)$  given by Eq. (4.5). Benchmark parameters from Sec. 4 are used to match the high frequency detection range of resonant cavity based detectors, such as ADMX. The above plot shows the characteristic strain as a function of frequency for the benchmark binary GA system, with the the peak frequency  $f_p = 1.07$  GHz visualized by the red dashed line.

where  $t_+(\omega) = \frac{\omega - \omega_c}{2|\Delta m|\gamma}$  donates the non-zero stationary point and the phase argument  $\Psi_+(\omega)$  is given by  $\Psi_+(\omega) = \omega r + \frac{(\omega - \omega_c)^2}{4|\Delta m|\gamma} - \frac{\pi}{4}$ , identical to the form we defined within Eq. (4.5). Substituting in  $Q(t)$  as detailed within [29], we obtain:

$$\tilde{h}_\times(f) = -\frac{2}{i}h_0 \cos \iota \sqrt{\pi} |\Delta m|^2 i e^{i\Psi_+(f)} \frac{\sqrt{z}}{|\Gamma| - i\pi(f - f_c)} e^{-\pi z} \exp\left[-2z \arctan\left(\frac{\pi(f - f_c)}{|\Gamma|}\right)\right] \quad (\text{A.30})$$

where we rewrote the frequency as  $f = \omega/2\pi$ . Comparing to Eq. (4.5):

$$\tilde{h}_+(f) = h_0(1 + \cos^2 \iota) \sqrt{\pi} |\Delta m|^2 i e^{i\Psi_+(f)} \frac{\sqrt{z}}{|\Gamma| - i\pi(f - f_c)} e^{-\pi z} \exp\left[-2z \arctan\left(\frac{\pi(f - f_c)}{|\Gamma|}\right)\right]$$

we notice that similar to isolated level transitions described within Sec. A.2, the two polarizations differ only by the inclination weighting and a relative phase of  $\pi/2$  given by the factor of  $-2/i$ . Figure 13 showcases the characteristic strain for the benchmark parameters from that produce UHF-GWs with frequency  $\sim 1$  GHz.

## References

- [1] A. Berlin, N. Blinov, P. Schuster and N. Toro, *Detecting high-frequency gravitational waves with microwave cavities*, *Phys. Rev. D* **105** (2022) 116011 [2112.11465].

- [2] N. Aggarwal et al., *Challenges and opportunities of gravitational-wave searches at mhz to ghz frequencies*, *Living Rev. Rel.* **24** (2021) 4 [[2011.12414](#)].
- [3] V. Domcke, C. Garcia-Cely and N.L. Rodd, *A novel search for high-frequency gravitational waves with low-mass axion haloscopes*, *Phys. Rev. Lett.* **129** (2022) 041101 [[2202.00695](#)].
- [4] R.D. Peccei and H.R. Quinn,  *$C_p$  conservation in the presence of instantons*, *Phys. Rev. Lett.* **38** (1977) 1440.
- [5] S. Weinberg, *A new light boson?*, *Phys. Rev. Lett.* **40** (1978) 223.
- [6] F. Wilczek, *Problem of strong  $p$  and  $t$  invariance in the presence of instantons*, *Phys. Rev. Lett.* **40** (1978) 279.
- [7] J. Preskill, M.B. Wise and F. Wilczek, *Cosmology of the invisible axion*, *Phys. Lett. B* **120** (1983) 127.
- [8] L.F. Abbott and P. Sikivie, *A cosmological bound on the invisible axion*, *Phys. Lett. B* **120** (1983) 133.
- [9] M. Dine and W. Fischler, *The not-so-harmless axion*, *Phys. Lett. B* **120** (1983) 137.
- [10] G. di Cortona, E. Hardy, J. Pardo Vega and G. Villadoro, *The qcd axion, precisely*, *JHEP* **01** (2016) 034 [[1511.02867](#)].
- [11] Y.B. Zel'dovich, *Generation of waves by a rotating body*, *JETP Lett.* **14** (1971) 180.
- [12] Y.B. Zel'dovich, *Amplification of cylindrical electromagnetic waves reflected from a rotating body*, *Sov. Phys. JETP* **35** (1972) 1085.
- [13] W.H. Press and S.A. Teukolsky, *Floating orbits, superradiant scattering and the black-hole bomb*, *Nature* **238** (1972) 211.
- [14] S. Detweiler, *Klein-gordon equation and rotating black holes*, *Phys. Rev. D* **22** (1980) 2323.
- [15] R. Brito, V. Cardoso and P. Pani, *Superradiance: New frontiers in black hole physics*, *Lect. Notes Phys.* **906** (2015) 1 [[1501.06570](#)].
- [16] A. Arvanitaki and S. Dubovsky, *Exploring the string axiverse with precision black hole physics*, *Phys. Rev. D* **83** (2011) 044026 [[1004.3558](#)].
- [17] A. Arvanitaki, M. Baryakhtar and X. Huang, *Discovering the qcd axion with black holes and gravitational waves*, *Phys. Rev. D* **91** (2015) 084011 [[1411.2263](#)].
- [18] M. Isi et al., *Stochastic gravitational-wave background from ultralight bosons*, *Phys. Rev. D* **99** (2019) 084042 [[1810.03812](#)].
- [19] K.K.Y. Ng et al., *Search for ultralight bosons in black hole spin measurements*, *Phys. Rev. D* **99** (2019) 043010 [[1901.00006](#)].
- [20] L. Tsukada et al., *First search for ultralight bosons with a stochastic gravitational-wave background*, *Phys. Rev. D* **99** (2019) 103015 [[1812.09622](#)].
- [21] L. Sun et al., *Search for continuous gravitational waves from boson clouds around spinning black holes*, *Phys. Rev. D* **102** (2020) 043020 [[2005.00342](#)].
- [22] B. Carr, F. Kühnel and L. Sandstad, *Primordial black holes as dark matter*, *Phys. Rev. D* **94** (2016) 083504 [[1607.06077](#)].
- [23] M. Raidal, V. Vaskonen and H. Veermäe, *Gravitational waves from primordial black hole mergers*, *JCAP* **09** (2017) 037 [[1707.01480](#)].
- [24] Y. Ali-Haïmoud and M. Kamionkowski, *Cosmic microwave background limits on accreting primordial black holes*, *Phys. Rev. D* **95** (2017) 043534 [[1612.05644](#)].
- [25] H. Yoshino and H. Kodama, *Bosenova collapse of axion cloud around a rotating black hole*, *Prog. Theor. Exp. Phys.* (2014) 043E02 [[1312.2326](#)].

- [26] H. Yoshino and H. Kodama, *The bosonova and axiverse*, *Class. Quant. Grav.* **32** (2015) 214001 [[1407.2030](#)].
- [27] D. Baumann, H.S. Chia and R.A. Porto, *Probing ultralight bosons with binary black holes*, *Phys. Rev. D* **99** (2019) 044001 [[1804.03208](#)].
- [28] D. Baumann, H.S. Chia, R.A. Porto and J. Stout, *Gravitational collider physics*, *Phys. Rev. D* **101** (2020) 083019 [[1912.04932](#)].
- [29] A. Kyriazis and F. Yang, *Gravitational waves from resonant transitions of tidally perturbed gravitational atoms*, *JHEP* **11** (2025) 062 [[2503.18121](#)].
- [30] Y. Chen et al., *Gravitational-wave signatures of ultralight bosons in extreme mass ratio inspirals*, *Phys. Rev. D* **101** (2020) 103008 [[1912.06605](#)].
- [31] J. Zhang, H. Yang and L. Lehner, *Binary dynamics with ultralight boson clouds*, *Phys. Rev. D* **101** (2020) 044020 [[1908.11286](#)].
- [32] G.M. Tomaselli and G. Bertone, *Resonant history of gravitational atoms in black hole binaries*, *Phys. Rev. D* **109** (2024) 044033 [[2303.12015](#)].
- [33] S. Hoof, D.J.E. Marsh, J. Sisk-Reynés, J.H. Matthews and C. Reynolds, *Getting more out of black hole superradiance: a statistically rigorous approach to ultralight boson constraints from black hole spin measurements*, *Monthly Notices of the Royal Astronomical Society* **546** (2025) staf1564 [[2406.10337](#)].
- [34] S. Hoof <https://github.com/sebhoof/bhsr>.
- [35] N. Siemonsen, T. May and W.E. East, *Modeling the black hole superradiance gravitational waveform*, *Phys. Rev. D* **107** (2023) 104003 [[2211.03845](#)].
- [36] T. May, W.E. East and N. Siemonsen, *Self-gravity effects of ultralight boson clouds formed by black hole superradiance*, *Phys. Rev. D* **111** (2025) 044062 [[2410.21442](#)].
- [37] M. Raidal, V. Vaskonen and H. Veermäe, *Formation of Primordial Black Hole Binaries and Their Merger Rates*, in *Primordial Black Holes*, C. Byrnes, G. Franciolini, T. Harada, P. Pani and M. Sasaki, eds. (2025), DOI [[2404.08416](#)].
- [38] S.R. Dolan, *Instability of the massive Klein-Gordon field on the Kerr spacetime*, *Phys. Rev. D* **76** (2007) 084001 [[0705.2880](#)].
- [39] T. Harada, C.-M. Yoo, K. Kohri, K.-i. Nakao and S. Jhingan, *Spins of primordial black holes formed in the matter-dominated phase of the Universe*, *Phys. Rev. D* **96** (2017) 083517 [[1707.03595](#)].